Dynamics of the [4Fe-4S] Cluster in *Pyrococcus furiosus* D14C Ferredoxin via Nuclear Resonance Vibrational and Resonance Raman Spectroscopies, Force Field Simulations, and Density Functional Theory Calculations

Devrani Mitra,[†] Vladimir Pelmenschikov,[‡] Yisong Guo,[†] David A. Case,[§] Hongxin Wang,[†,||] Weibing Dong,[†] Ming-Liang Tan,[⊥] Toshiko Ichiye,[⊥] Francis E. Jenney, Jr.,[@] Michael W. W. Adams,[#] Yoshitaka Yoda,[∇] Jiyong Zhao,[●] and Stephen P. Cramer*,[†,||]

[†]Department of Applied Science, University of California, Davis, California 95616, United States

[‡]Institut für Chemie, Technische Universität Berlin, Strasse des 17. Juni 135, 10623 Berlin, Germany

[§]Department of Chemistry and Chemical Biology and BioMaPS Institute, Rutgers University, Piscataway, New Jersey 08854, United States

[||]Physical Biosciences Division, Lawrence Berkeley National Laboratory, Berkeley, California 94720, United States

[⊥]Department of Chemistry, Georgetown University, Washington, D.C. 20057, United States

[@]Georgia Campus, Philadelphia College of Osteopathic Medicine, Suwanee, Georgia 30024, United States

[#]Department of Biochemistry and Molecular Biology, University of Georgia, Athens, Georgia 30602, United States

[∇]JASRI, SPring-8, 1-1-1 Kouto, Mikazuki-cho, Sayo-gun, Hyogo 679-5198, Japan

[●]Advanced Photon Source, Argonne National Laboratory, Argonne, Illinois 60439, United States

S *Supporting Information*

ABSTRACT:
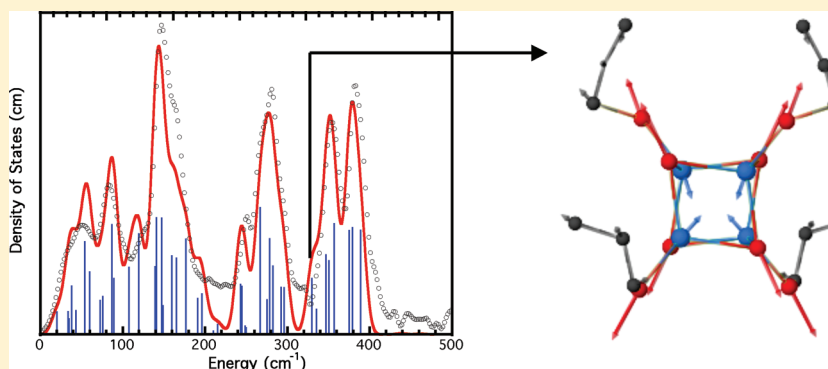
We have used ^{57}Fe nuclear resonance vibrational spectroscopy (NRVS) to study oxidized and reduced forms of the [4Fe-4S] cluster in the D14C variant ferredoxin from *Pyrococcus furiosus* (*Pf* D14C Fd). To assist the normal-mode assignments, we conducted NRVS with D14C ferredoxin samples with ^{36}S substituted into the [4Fe-4S] cluster bridging sulfide positions, and a model compound without ligand side chains, $(Ph_4P)_2[Fe_4S_4Cl_4]$. Several distinct regions of NRVS intensity are identified, ranging from "protein" and torsional modes below 100 cm^{-1}, through bending and breathing modes near 150 cm^{-1}, to strong bands from Fe−S stretching modes between 250 and ∼400 cm^{-1}. The oxidized ferredoxin samples were also investigated by resonance Raman (RR) spectroscopy. We found good agreement between NRVS and RR frequencies, but because of different selection rules, the intensities vary dramatically between the two types of spectra. The ^{57}Fe partial vibrational densities of states for the oxidized samples were interpreted by normal-mode analysis with optimization of Urey−Bradley force fields for local models of the [4Fe-4S] clusters. Full protein model calculations were also conducted using a supplemented CHARMM force field, and these calculations revealed low-frequency modes that may be relevant to electron transfer with *Pf* Fd partners. Density functional theory (DFT) calculations complemented these empirical analyses, and DFT was used to estimate the reorganization energy associated with the $[Fe_4S_4]^{2+/+}$ redox cycle. Overall, the NRVS technique demonstrates great promise for the observation and quantitative interpretation of the dynamical properties of Fe−S proteins.

Iron−sulfur clusters are among the most common and ancient prosthetic groups in proteins.[1,2] The [4Fe-4S] versions,

initially discovered as electron transfer agents,[3] have since been shown to function in catalysis, cofactor biosynthesis, Fe storage, regulation of gene expression and enzyme activity, DNA repair and as structural components of proteins.[4−6] A recent survey of Fe−S proteins found at least 35 distinct protein folds containing [4Fe-4S] clusters, with a relatively constant rate of discovery of new folds since 1995.[7]

The hyperthermophilic Archaeon *Pyrococcus furiosus* (*Pf*)[8] contains an ∼7.5 kDa ferredoxin (Fd) with a single [4Fe-4S] cluster that is coordinated by three cysteine ligands (C11, C17, and C56) and one aspartate ligand (D14).[9] This protein plays a central role in *Pf* metabolism, serving as an electron acceptor in fermentation and as an electron donor in hydrogen evolution pathways. Because of its small size and high stability even at 95 °C, as well as the ready interconversion between [4Fe-4S] and [3Fe-4S] clusters, *Pf* Fd has been extensively investigated by site-directed mutagenesis,[10−12] along with electrochemical, EPR, and resonance Raman (RR) studies[12] and theoretical calculations.[13−15] An X-ray diffraction crystal structure for the *Pf* D14C Fd variant in the oxidized $[Fe_4S_4]^{2+}$ form has been determined.[16] The structure has been described as the same fold observed for other monocluster ferredoxins, with two double-stranded antiparallel β-sheets and two α-helices, depicted using VMD[17] (Chart 1). In the *Pf* D14C variant, the exchangeable Fe is also coordinated by cysteine and is within 13 Å of solvent water molecules. The rest of the [4Fe-4S] cluster is blocked from direct contact with solvent and coordinated by NH−S hydrogen bonds.

In model compounds and in proteins, [4Fe-4S] clusters usually exhibit distortions from tetrahedral symmetry.[18−20] High-resolution crystal structures of [4Fe-4S] model complexes frequently reveal tetragonally compressed clusters, with four short and eight long Fe−S bonds and approximate D_{2d} symmetry.[18,19] An alternate description is that the bridging S tetrahedron is elongated along a z-axis, while the Fe tetrahedron is compressed along the same axis.[21] This lowering of symmetry is commonly assigned to a multicenter Jahn−Teller distortion,[22] but it has also been argued that the distortion comes from packing effects on the cluster side chains, which in turn affect the availability of sulfur lone pairs for interaction with Fe d orbitals.[21] The synthesis of strictly tetrahedral [4Fe-4S] clusters tends to support the notion that these distortions are not intrinsic to the cubane structure but arise from external forces.[23,24]

Resonance Raman spectroscopy has been an important tool for the elucidation of the structure and dynamics of [4Fe-4S] clusters, including differences between [4Fe-4S] clusters in low-potential ferredoxins and high-potential iron proteins (HiPIPs).[25−27] RR spectroscopy has also been used to probe [4Fe-4S] → [3Fe-4S] interconversion,[28−30] reductive coupling of [2Fe-4S] to [4Fe-4S] clusters on the IscU scaffold protein,[31] partial [4Fe-4S] → [2Fe-4S] transformation in the nitrogenase Fe protein,[32] and changes in electron localization in ferredoxin: thioredoxin reductase.[33]

As with other vibrational spectroscopies, the symmetry of a cluster can be revealed by the number of nondegenerate normal modes.[34] For [4Fe-4S] clusters, descent from T_d to D_{2d} symmetry by a tetragonal distortion is predicted to split the RR-active normal modes, according to $E \rightarrow A_1 + B_1$, $T_1 \rightarrow A_2 + E$, and $T_2 \rightarrow B_2 + E$ transitions.[26,35] The solid state spectrum for the model $(Et_4N)_2[Fe_4S_4(SCH_2Ph)_4]$ exhibits such apparent E/B_2 splitting features at 359/367 and 243/249 cm^{-1}, respectively.[26] These features coalesce into single peaks at 360 and 244 cm^{-1} in the solution spectrum, and this change has been used to argue for a tetrahedral structure in this state.[26] Similar E/B_2 splittings were assigned early on for *Clostridium pasteurianum* (*Cp*) Fd[25,26] and later for *Clostridium acidi-urici* (*Ca*) ferredoxins.[27] Initially, the absence of such splitting in the HiPIP RR spectrum was interpreted as evidence of a more tetrahedral geometry.[26] However, subsequent higher-resolution HiPIP spectra revealed that such features were indeed split,[27] confirming that, in accord with their crystal structures, HiPIP clusters also possess a distorted nontetrahedral geometry.

The previously reported RR spectrum for *Pf* D14C Fd is very similar to those of other all-cysteinyl-ligated ferredoxins.[12] An apparent E/B_2 splitting of features at 354/363 cm^{-1} has been assigned, on the basis of analogy with previous *Cp* Fd work. Although a tetragonal distortion similar to those seen in high-resolution structures for *Bacillus thermoproteolyticus*[36] and *Ca*[37] ferredoxins might have been expected, the crystal structure of oxidized *Pf* D14C Fd at 1.70 Å resolution[16] reveals an only slightly distorted $[Fe_4S_4]^{2+}$ core with approximate D_{2d} symmetry for the $Fe_4S^b_4S^t_4$ (where S^b and S^t stand for bridging and terminal sulfurs, respectively) portion of the $Fe_4S_4Cys_4$ site (Chart 1). Individual Fe−Fe distances range from 2.71 to 2.75 Å, while the Fe−S^b bond lengths range from 2.29 to 2.34 Å. The variety of orientations of the cysteine side chain carbons and Fe−S−C−C dihedral angles lowers the true site symmetry to

Chart 1. (a) VMD[17] Cartoon Representation of the $[Fe_4S_4]^{2+}$ Form of Oxidized *Pf* D14C Ferredoxin (PDB entry 2Z8Q) and (b) Close-Up of the Crystallographically Observed Cluster Site (color) Compared to a Hypothetical $Fe_4S_4(SCCC)_4$ Model with C_2 Symmetry (gray)

(a)

(b)
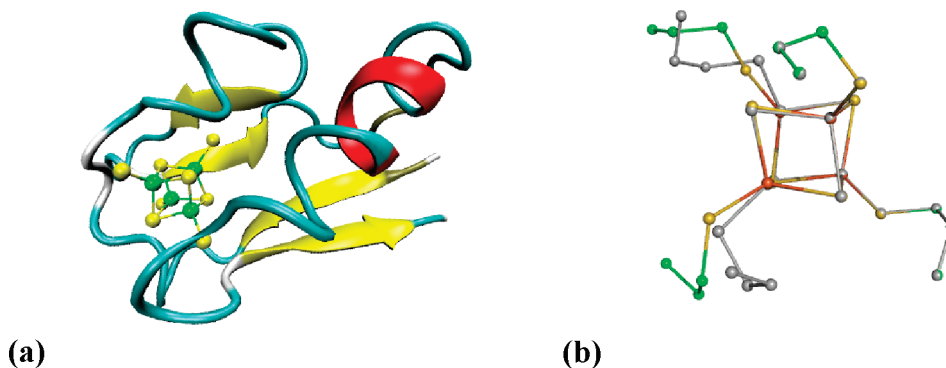
C_1, but as illustrated in Chart 1, C_2 symmetry remains a useful approximation. As for hydrogen bonding to the cluster, in oxidized *Pf* D14C Fd there are eight NH···S interactions, the same number observed for other well-studied ferredoxins.[38,39]

Several groups have developed empirical force fields to model the dynamics of [4Fe-4S] clusters. Spiro and co-workers used a D_{2d} $Fe_4S^b{}_4S^t{}_4$ model, with a Urey—Bradley force field (UBFF) and Badger's rule adjustment of Fe—S stretching force constants, to successfully reproduce most of the Fe—S stretching frequencies.[26] As with rubredoxin,[40−42] the significance of Fe—S—C—C dihedral angles in the coupling between Fe—S stretching and S—C—C bending[43] was emphasized.[12,27] The conformational differences between proteins and models were also proposed to account for differences in mode ordering and mode frequencies.[26] In an analysis of $(Bu_4N)_2[Fe_4S_4(SCH_3)_4]$ using a D_{2d} $Fe_4S^b{}_4(S^tC)_4$ model, Kern and co-workers augmented the Spiro force field with S—C stretching, Fe—C nonbonding interactions, and bend and torsion force constants involving the terminal ligands.[21] Although the importance of coupling between Fe—S stretch and S—C—C bend motions was noted in both studies, extended side chains were not included in either set of calculations. Later, thiolate ligand orientation effects were explicitly included in simulations of aconitase spectra.[29] In our NRVS analysis of $(Bu_4N)_2[Fe_4S_4(SPh)_4]$, we employed an empirical force field and idealized structures from T_d to C_1 symmetry,[44] and the results were compared with results from DFT calculations.[44] Somewhat different force fields have been employed in molecular dynamics calculations for [4Fe-4S] clusters in HiPIPs[45] and ferredoxins.[46] These force fields, for example, CHARMM and AMBER, employ long-distance Coulomb and Lennard-Jones terms that are absent from the Urey—Bradley force fields.

Compared to those of their oxidized partners, the dynamic properties of reduced [4Fe-4S] sites in proteins remain unexplored, because neither RR nor FT-IR has succeeded in probing the $[Fe_4S_4]^+$ redox level. The few structures available for $[Fe_4S_4]^+$ clusters indicate only modest structural changes, but we know nothing about changes in force constants. An improved understanding of the dynamics of all redox levels would be useful for predictions about structure and function in Fe—S proteins. For this reason, we have examined *Pf* D14C Fd by a combination of resonance Raman (RR) spectroscopy and nuclear resonance vibrational spectroscopy (NRVS).

NRVS has become a popular technique for probing the dynamics of Fe in metalloproteins,[47,48] and the essential physics of this technique have been reviewed.[49,50] The measurement involves scanning an extremely monochromatic X-ray beam through a nuclear resonance. As with an IR or RR spectrum, NRVS reveals vibrational normal modes, but with different selection rules. Specifically, the NRVS intensity for a given normal mode is related to the motion of the resonant nucleus (in this case ^{57}Fe) along the direction of the incident X-ray beam.[48,51] For a randomly oriented sample, the normalized excitation probability $S(\bar{v})$ for a transition involving normal mode α at frequency $\bar{v}_\alpha$ is directly proportional to Fe-mode composition factor $e_{Fe,\alpha}{}^2$:[51,52]

$$S(\bar{v}_\alpha) \propto e_{Fe,\alpha}^2 = \frac{m_{Fe}r_{Fe,\alpha}^2}{\sum_i m_i r_{i\alpha}^2} \qquad (1)$$

where m_i and $r_{i\alpha}{}^2$ are the mass of atom i and its mean square motion in mode α, respectively, and $\bar{v}_\alpha$ is the difference between the photon energy and the recoil-free nuclear resonance energy. The results are typically reported as an ^{57}Fe-centered partial vibrational density of states (PVDOS), $D_{Fe}(\bar{v})$, using a line shape function $\mathscr{L}(\bar{v} - \bar{v}_\alpha)$ to account for instrumental and lifetime broadening:[51,53]

$$D_{Fe}(\bar{v}) = \sum_\alpha e_{Fe,\alpha}^2 \mathscr{L}(\bar{v} - \bar{v}_\alpha) \qquad (2)$$

Here we report the ^{57}Fe NRVS spectra for oxidized and reduced ^{57}Fe-enriched *Pf* D14C Fd, both with natural abundance S and with ^{36}S in the bridging sulfide positions. RR spectra for both oxidized isotopomers are also presented. By combining constraints from NRVS and RR spectra and their ^{36}S isotope shifts, we were able to refine a Urey—Bradley force field for the oxidized site. The results are compared with previous RR and molecular mechanics analyses of [4Fe-4S] ferredoxins and model compounds. The new force field reproduces the high-frequency stretching modes, which has been done before, as well as the lower-frequency bending and torsional modes, which have not been quantitatively included in previous studies.

Furthermore, because the protein environment of the [4Fe-4S] cluster is key to its biological function, we extended the dynamical simulations to include the entire protein by means of a supplemented CHARMM force field. Finally, to complement these empirically based approaches, we also interpreted the spectra using DFT calculations. Overall, the results improve our understanding of the dynamics of [4Fe-4S] clusters, their coupling to the protein matrix, and the force constant changes and reorganization energies associated with redox activity.

■ METHODS

Model Compound Preparation. $(Ph_4P)_2(^{57}Fe_4S_4Cl_4)$ was prepared by literature methods.[54] Briefly, $^{57}FeCl_2$ was first prepared from reaction of metallic ^{57}Fe (100 mg) with HCl in methanol, concentrated, and cooled to −20 °C.[55] White crystals of $[Fe(MeOH)_x]Cl_2$ were obtained. The crystals were heated at 180 °C in vacuo for several hours to a constant weight. A Schlenk flask was prepared with a mixture of anhydrous $^{57}FeCl_2$ (65 mg, 0.51 mmol), KSPh (112 mg, 0.76 mmol), $(PPh_4)Cl$ (95 mg, 0.25 mmol), and elemental sulfur (20 mg, 0.63 mmol). Acetonitrile (5 mL) was then added with continuous stirring. After 45 min, the solution was filtered to remove KCl and unreacted sulfur and crystallized from ether. After several days, the solution exhibited deposition of a black crystalline solid. The product, 55 mg of $(PPh_4)_2(^{57}Fe_4S_4Cl_4)$, was isolated by filtration, washed twice with ether, and dried in vacuo.

Protein Purification and Sample Preparation. Recombinant *Pf* D14C Fd was expressed in *Escherichia coli* and purified using the same expression vector and conditions described previously.[11] For preparation of protein with ^{36}S- and ^{57}Fe-substituted [4Fe-4S] clusters, the protein was reconstituted in a manner similar to that described previously.[56] The protein (116 mg) was first denatured by addition of cHCl (c_f = 1.2 M), EDTA (c_f = 0.5 M), and 2-mercaptoethanol (2-ME) (c_f = 0.2 M). The sample was incubated while being slowly swirled at 37 °C for 4 h, resulting in precipitation and loss of the brown color. The protein was pelleted by centrifugation at 18000g and resuspended in 0.5 M Tris (pH 8.5) and 0.5 M 2-ME. This precipitation was repeated twice. The final (white) pellet was washed first by resuspension in 10 mL of ice-cold 100% acetone and centrifugation again, and then briefly with HPLC grade water, and dried.

The pellet was dissolved in 0.5 M Tris (pH 8.0) and 100 mM 2-ME to a concentration of ~6 mg of protein/mL and diluted to a concentration of ~2 mg of protein/mL in 0.5 M Tris (pH 8.0) and 100 mM dithiothreitol.

To prepare the iron used in reconstitution, we dissolved 11.2 mg of elemental ^{57}Fe (95%) in 90 μL of *aqua regia* (3:1 HCl/HNO$_3$ mixture), resulting in a completely dissolved, bright yellow solution. This solution (20-fold molar excess over the protein) was injected into an anaerobic vial containing the solubilized protein (~2 mg/mL) while being stirred under Ar. For reconstitution with natural abundance S, Na$_2$S was added (20-fold molar excess over protein).

For reconstitution with ^{36}S, the ^{36}S sulfide was prepared essentially as described in refs 57 and 58, in which elemental S was reduced to the S^{2-} oxidation level by being heated in a hydrogen atmosphere. In brief, 2.4 mg (~67 μmol) of ^{36}S was extensively degassed in each of four sealed 12 mL vials and then flushed with pure H$_2$. The vial was heated over a low flame until all visible sulfur, which had sublimed onto the sides of the vial upon heating, had disappeared. After the sample had cooled to room temperature, some sulfur reappeared on the glass, and the vials were heated again, which was enough to reduce all the sulfur to sulfide. When the ^{36}S sulfide was prepared, 400 μL of 50 mM Tris (pH 8.5) with 50 mM DTT was injected and used to carefully rinse the entire inside of the vial. Approximately 1 μmol of ferredoxin (~8 mg of protein mixed with ^{57}Fe, 20-fold excess of ^{36}S over protein) was then injected into each vial, the contents of which began turning brown immediately. The contents of the four vials were combined into one, and the solution was stirred overnight at room temperature under Ar.

The next day, the reconstituted proteins were diluted into 200 mL of degassed water and loaded onto a DEAE-FF anion exchange column (GE Healthcare, Piscataway, NJ) equilibrated in buffer A [50 mM Tris (pH 8.0)], block eluted with 500 mM NaCl in buffer A, and concentrated by ultrafiltration. For all protein samples described below, we produced the air-oxidized form of the protein by washing it extensively in 100 mM Tris (pH 8.0) followed by ultracentrifugation with Amicon Ultra-4 5 kDa NMWL filters (Millipore, Billerica, MA). For the reduced samples, the protein was extensively degassed and flushed with Ar and then reduced by being washed several times in an anaerobic chamber with a Microcon YM3 kDa NMWL (Millipore) with 20 mM sodium dithionite in 100 mM Tris (pH 8.0).

Mössbauer Spectroscopy. As *Pf* Fd can undergo interconversion between [4Fe-4S] and [3Fe-4S] forms, the cluster nuclearity and redox status for all samples were monitored by conventional Mössbauer spectroscopy. The spectra were recorded at 78 K under zero magnetic field using a sine-wave-acceleration spectrometer with an Oxford OptistatDN cryostat. The spectrometer consists of a Wissel 1200 Mössbauer velocity drive unit, a LND-45431 proportional counter, and a room-temperature ^{57}Co/Rh source. Isomer shifts are quoted relative to 25 μm α-Fe foil at 298 K. Mössbauer spectral simulations were conducted using the NORMOS-90 software package (Wissenschaftliche Elektronik GmbH). The Mössbauer spectra and simulations are given in Figure S1 of the Supporting Information.

Nuclear Resonance Vibrational Spectroscopy. For NRVS measurements, samples were loaded into 3 mm × 7 mm × 1 mm (interior dimensions) Lucite cuvettes. ^{57}Fe NRVS spectra were recorded using published procedures[48] on multiple occasions at

beamline 3-ID at the Advanced Photon Source (APS)[59] and beamline BL09XU at SPring-8.[60] Fluxes were on the order of 3 × 10^9 photons/s in a 1.1 eV bandpass. During NRVS measurements, samples were kept at low temperatures using liquid He cryostats. Temperatures were calculated from the ratio of anti-Stokes to Stokes intensity via $S(-E) = S(E) \exp(-E/kT)$. Although the temperature reading at the sensor was ~6 K, the real sample temperature obtained from the spectral imbalance analysis was ~100–120 K. Nuclear fluorescence and delayed Fe K fluorescence were recorded with a single 1 cm^2 square avalanche photodiode (APD) at the APS and with an APD array at SPring-8. Each scan took ~40 min, and all scans were added and normalized to the intensity of the incident beam. Each final protein spectrum represents ~12–24 h of measurement. The (Ph$_4$P)$_2$[Fe$_4$S$_4$Cl$_4$] model data represent the average of three scans from each facility.

Resonance Raman Spectroscopy. RR spectra were recorded in a backscattering geometry from frozen drops of *Pf* D14C Fd solutions on a Au-plated Cu coldfinger inside an Oxford Optistat-DN liquid nitrogen cryostat at 77 K. The excitation source was a Coherent Innova-2 Ar$^+$/Kr$^+$ laser, using a power of ~35 mW and operating at 488 nm. The spectra were recorded with a Spex model 1877 triple Raman spectrograph, using a cooled Spectrum One 594 CCD detector. The spectra were calibrated using peaks at 218 and 314 cm^{-1} in a room-temperature CCl$_4$ sample, as well as 85.1, 153.8, and 219.1 cm^{-1} peaks in elemental sulfur. To improve the accuracy of the Raman calibration, the entire stretching region spectrum (180–480 cm^{-1}) was recorded simultaneously as one region. The slits were set to 0.15 mm to achieve ~6 cm^{-1} resolution. Each spectrum represents ~45–60 h of measurement.

Empirical Force Field Normal-Mode Calculations. Empirical normal-mode calculations were conducted with a UBFF using VIBRATZ.[61] The crystal structure for oxidized *Pf* D14C Fd was obtained from the Protein Data Bank.[16] Because there was no crystal structure for the reduced Fd, a plausible structure was generated by mimicking the core bond lengths of the reduced model compound, (Et$_4$N)$_3$[Fe$_4$S$_4$(SCH$_2$Ph)$_4$].[18] The four shorter Fe–S^b bond lengths and the eight longer Fe–S^b bond lengths were fixed at 2.302 and 2.33 Å, respectively, while Fe–S^t bond distance were kept at 2.297 Å, using the MOLSTART Java application program.

For the "full protein" calculations, H atom coordinates were built using the HBUILD facility of CHARMM 33.[62] The systems contain 968 protein atoms and 55 crystal water molecules. The force field parameters consisted of the CHARMM22 all-atom parameters[62] and additional parameters for the [4Fe-4S] cluster as initially obtained from the "local site" optimization. To obtain a structure for the normal-mode calculation, it was necessary to refine the X-ray crystal structures (PDB entry 2Z8Q)[28–30] to a minimum energy conformation. Constraints were introduced during the minimizations that led to a minimum energy structure close to the crystal structure, and a mass-weighted atomic harmonic potential was applied to each heavy atom. The systems were energy-minimized by 1000 steps of the steepest descent method followed by successive sets of Adopted Basis Newton–Raphson (ABNR) minimizations (500 steps each) with the constraints reduced and the reference structure updated each set; the final constraint constant was 0.05 kcal mol^{-1} Å^{-2} per atomic mass. The normal-mode calculations were then performed without constraints using the VIBRan module in CHARMM 33.[62] For comparison with the experimental spectra,

Gaussian functions were calculated centered around each ω_α, the frequency of mode α, using an 8 cm^{-1} full width at half-maximum (fwhm) and amplitude proportional to $e_{j\alpha}^2$. The ^{57}Fe PVDOS was then obtained by summing these Gaussian functions over all modes.

"Degree of Collectivity" Calculations. The degree of collectivity "κ", first proposed by Bruschweiler,[63] was calculated by the equation given by Tama and Sanejouand,[64] except that the Fe and S atoms of the cluster were included in the summation along with all non-hydrogen protein atoms:

$$\kappa = \frac{1}{N} \exp\left(-\sum^N \alpha \Delta R_i^2 \log \Delta R_i^2\right) \quad (3)$$

where α is a normalization factor chosen so that $\Sigma^N \alpha \Delta R_i^2 = 1$.

DFT Calculations. The molecular model for the density functional theory (DFT) calculations was based on the 1.7 Å resolution crystal structure of Pf D14C Fd,[16] with initial coordinates extracted from PDB entry 2Z8Q. The four cysteinyl ligands to the [4Fe-4S] core were modeled using ethyl thiolates, $CH_3CH_2S^-$, taken exactly as in the X-ray structure (α- and β-carbons and the γ-sulfur of Cys).

The four Fe sites of the [4Fe-4S] cluster were treated as two pairs of high-spin Fe centers, coupled antiferromagnetically to produce a low-spin [2Fe↑:2Fe↓] broken symmetry (BS) $S = 0$ spin state[22] for the diamagnetic oxidized form, $[Fe_4S_4]^{2+}$, and an $S = 1$ spin state for the reduced form, $[Fe_4S_4]^+$. The BS electronic structures were constructed using an option to assign a number of unpaired α/β-electrons to Fe atomic fragments, as implemented in JAGUAR 7.5.[65] These starting BS densities were further used to proceed with the geometry optimizations and analytic Hessian calculations using GAUSSIAN 03.[66] For all the calculations, the PW91[67] density functional was used with the LACV3P** basis set, as implemented in JAGUAR. For the first- and second-row elements, LACV3P** implies a 6-311G** triple-ζ basis set, including the polarization function. For the Fe atom, LACV3P** uses the Los Alamos effective core potential (ECP), and the valence part is essentially of triple-ζ quality.

Three approaches to the geometry optimization of $[Fe_4S_4(SCH_2CH_3)_4]^{2-}$ oxidized form model and its subsequent spectroscopy interpretation by DFT were considered: (i) all atoms relaxed, (ii) α-carbons of Cys ligands fixed to their X-ray positions, and (iii) both α- and β-carbons of Cys fixed. The intermediate fixation scheme (ii) is implied in the text, if not otherwise mentioned.

The ^{57}Fe isotope mass was used for the normal-mode analysis following Hessian calculations. On the basis of normal-mode analysis, NRVS and kinetic energy distribution (KED) spectra were generated using Q-SPECTOR, an in-house Python tool for analysis of the vibrational normal modes calculated by various computational chemistry software (here, GAUSSIAN). To match the width of the experimental spectra, the simulated spectra were broadened by convolution with a 7 cm^{-1} (fwhm) Gaussian line shape.

The calculation of the self-exchange inner-sphere contribution λ_i to the reorganization energy of the [4Fe-4S] cluster was conducted in a manner following others:[68,69]

$$\lambda_i = \lambda_{ox} + \lambda_{red}$$

$$\lambda_{ox} = E(Ox^{Ox}) - E(Red^{Ox}) \quad (4)$$

$$\lambda_{red} = E(Red^{Red}) - E(Ox^{Red})$$

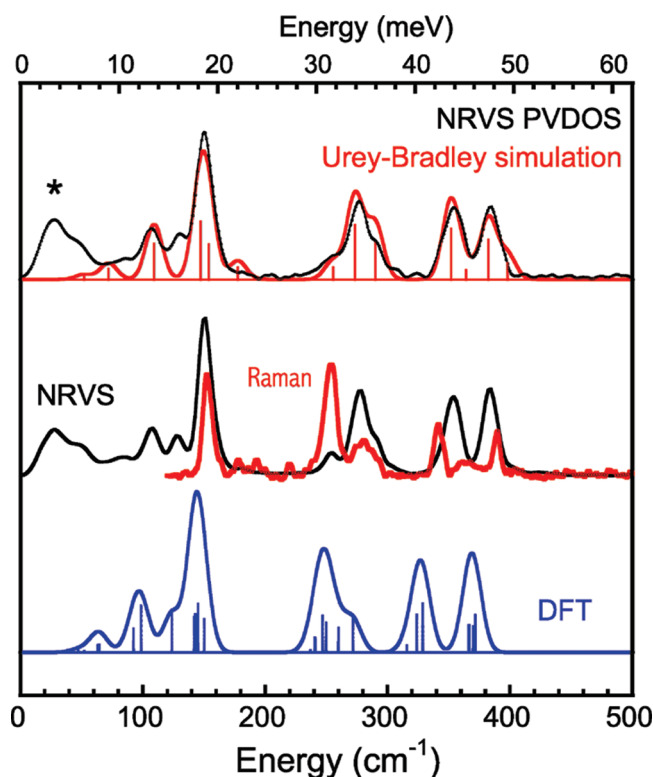**Figure 1.** Data and simulations for $(Ph_4P)_2[^{57}Fe_4S_4Cl_4]$. From top to bottom: experimental ^{57}Fe PVDOS (black line) and Urey–Bradley simulation (red line), experimental ^{57}Fe PVDOS (black line) compared with the resonance Raman spectrum (red line), and DFT calculations for $[^{57}Fe_4S_4Cl_4]^{2-}$ (blue line). The asterisk indicates the low-frequency region of acoustic modes not included in the calculations. Sticks show frequencies and relative intensities of calculated normal modes before linewidth broadening.

where λ_{ox}, the reorganization energy during oxidation, is the difference between the energies of the oxidized complex $[Fe_4S_4(SCH_2CH_3)_4]^{2-}$ in its equilibrium geometry (Ox^{Ox}) and the oxidized complex in the equilibrium geometry of the reduced complex (Red^{Ox}). Similarly, λ_{red}, the reorganization energy during reduction, is the difference between the energies of the reduced complex $\{[Fe_4S_4(SCH_2CH_3)_4]^-\}$ in its equilibrium geometry (Red^{Red}) and the reduced complex in the equilibrium geometry of the oxidized complex (Ox^{Red}).

■ RESULTS

$[Fe_4S_4Cl_4]^{2-}$, **a Simple Case.** Before addressing the relatively complex spectra of [4Fe-4S] clusters in proteins, we compare RR and NRVS spectra and analysis methods on a simpler system with fewer atoms and higher symmetry ($[Fe_4S_4Cl_4]^{2-}$). The vibrational modes for this cluster have been analyzed in T_d symmetry using IR and RR data;[35] here we compare the resonance Raman and NRVS data for the ^{57}Fe-substituted complex.

As shown in Figure 1, one often observes very different relative intensities for the same modes in RR and NRVS spectra. In the resonance Raman spectrum, modes are strong when the molecular geometry changes significantly in the electronic excited state, whereas in the NRVS spectrum, normal modes are strong when there is a significant amount of Fe motion in the vibrational ground state. Another major difference in the two spectra is that

Table 1. Mode Assignments and Calculated and Observed Frequencies and ^{36}S Isotope Shifts for Oxidized *Pf* D14C Fd

symmetry and mode label			*Cp*, RR[26]		*Pf* ^{57}Fe D14C Fd, RR		*Pf* ^{57}Fe D14C Fd, NRVS		calculated *Pf* D14C Fd values in D_{2d} (C_2) symmetry		
T_d	D_{2d}	C_2	ν (cm^{-1})	$\Delta\nu$, ^{34}S (cm^{-1})	ν (cm^{-1})	$\Delta\nu$, ^{36}S (cm^{-1})	ν (cm^{-1})	$\Delta\nu$, ^{36}S (cm^{-1})	ν (cm^{-1})	$\Delta\nu$, ^{36}S (cm^{-1})	e_{Fe}^{2}
A_1^t	A_1^t	A	395	3.9	391	9	390	6	389.0 (382.3)	6.2 (0.8)	0.424 (0.413)
T_2^b	B_2^b	B	380	5.6	381	12	382	14	379.0 (376.7)	6.2 (11.2)	0.435 (0.36)
	E^b	B			375	9	383	11	375.3 (384.0)	7.5 (12.8)	0.422 (0.657)
T_2^t	E^t	B	363	2.0	359	10	356	2.2	347.0 (350.3)	7.5 (2.7)	0.324 (0.837)
	B_2^t	A	351	0.7	349	7	353	10	357.0 (354.7)	1.2 (3.1)	0.45 (0.465)
A_1^b	A_1^b	A	338	7.0	336	15	335.5	8	335.5 (336.6)	11.8 (13)	0.102 (0.127)
E^b	A_1^b	B	298	4.9	297	8	297	7	296.0 (284.1)	9.6 (6.8)	0.190 (0.55)
	B_1^b	B	276	4.5	281	7	285	7	292.7 (279.0)	10.7 (7.5)	0.192 (0.504)
T_1^b	E^b	A	276	4.5	281	7	281	12	282.7 (276.7)	7.2 (7.3)	0.278 (0.972)
	A_2^b	A	(266)	4.0	267.5	9.0	267.0	8	267.0 (269.8)	6.3 (6.8)	0.516 (0.533)
T_2^b	B_2^b	A	251	6.2	250.5	11.5	251	10	248.9 (250.0)	3.6 (8.9)	0.033 (0.076)
	E^b	B	–	–	250.5	11.5	248	9	244.9 (245.6)	9.2 (9.3)	0.196 (0.289)
T_2^b	B_2^b	A	145	–	151	0.8	150.3	1.0	149.0 (150.0)	0.4 (1.9)	0.116 (0.292)
	E^b	B	–	–	146	1.0	147.0	2.0	147.5 (146.7)	1.8 (2.2)	0.473 (0.626)

the RR data have a resolution on the order of 6 cm^{-1} or 0.75 meV, while our NRVS data are currently broader by almost a factor of 2. This is not an intrinsic difference but merely the current resolution available at most synchrotron sources. Finally, the NRVS data have their strongest features in the bending region around 150 cm^{-1} and exhibit distinct features down to ~50 cm^{-1}, whereas in the Fe–S cluster RR data, the Fe–S stretching modes are usually the strongest features.

Empirical Force Field Analysis of [Fe$_4$S$_4$Cl$_4$]$^{2-}$. In T_d symmetry, there should be five primarily Fe–S^b stretching modes, involving A_1, T_1, T_2, and E symmetries, as well as A_1 and T_2 stretching modes from the terminal ligands.[26] All except the terminal ligand A_1 mode have been identified in the resonance Raman or IR data.[35] Because of the lower resolution, several of these modes are unresolved in the NRVS data. To simulate the NRVS, we employed the force field used by Kern and co-workers[35] with slight variations (Table 1). The best simulation for this complex in T_d shows good correspondence with the experimental spectrum (Figure 1).

The assignments in the bending region of the [Fe$_4$S$_4$Cl$_4$]$^{2-}$ NRVS spectrum in the low-frequency region are relevant to the subsequent *Pf* Fd analysis. The width of the 150 cm^{-1} feature is ~20 cm^{-1}, approximately half of that seen for the ferredoxin via NRVS. The T_d simulation has only two peaks in this region, a T_2 mode at 148 cm^{-1} and an E symmetry Fe breathing mode at 154 cm^{-1}. The RR and IR data in the previous report support this assignment.[35] Although Kern and co-workers proposed that the main peak corresponded to the A_1 Fe breathing mode, this lower-energy feature is seen in both the IR and RR spectra, consistent with a T_2 assignment. The higher-energy feature disappears in the IR spectrum, consistent with an E assignment for this mode.[35] We shall see below how addition of more side chain atoms further splits this region.

The only significant discrepancies between the T_d Urey–Bradley calculation and NRVS are the observed low-energy peak at 128 cm^{-1} and the predicted (but not observed) peak at 177 cm^{-1}. The predicted band is the A_1 Fe breathing mode derived from the T_d force field. Previous work by Kern and co-workers predicted breathing-mode frequencies between 153 and 177 cm^{-1} for [Fe$_4$S$_4$Cl$_4$]$^{2-}$,[35] while Czernuszewicz and co-workers assigned

features at 165 cm^{-1} in a model compound and *Cp* ferredoxin spectra to this A_1 mode.[26] However, the PVDOS for [Fe$_4$S$_4$Cl$_4$]$^{2-}$ does not show the expected intensity in this region.

DFT Analysis of [Fe$_4$S$_4$Cl$_4$]$^{2-}$. Although empirical force fields can successfully reproduce the observed Raman frequencies and PVDOS, they come with the standard baggage of model dependence, parameter correlation, and limited transferability. For complicated cases such as enzyme intermediates, it would also be valuable to have a procedure for computing spectra of hypothetical structures for comparison with experimental data. We therefore investigated how well the spectra could be calculated from first principles using DFT, and the calculation result from [Fe$_4$S$_4$Cl$_4$]$^{2-}$ NRVS is also shown in Figure 1.

Overall, the agreement between theory and experiment is good. DFT generally captured the major peak intensities. The calculated peak positions were generally low by 4–8%, which is common for such predictions. Representative values are calculated and observed peaks at 143 and 150 cm^{-1}, 326 and 353 cm^{-1}, and 368 and 383 cm^{-1}, respectively. The only serious disagreement was the relative intensity of peaks in the 250–280 cm^{-1} region.

Apart from the known frequency shifts, the only significant difference between the DFT and UB predictions is the location of the A_1 Fe breathing mode. The DFT calculation predicts a symmetric mode at 124 cm^{-1}, close to an observed peak at 128 cm^{-1}, but 53 cm^{-1} lower than the Urey–Bradley value. It is perhaps surprising that an issue as simple as the assignment of the A_1 Fe breathing mode remains unresolved.

***Pf* D14C Fd Spectra.** The NRVS-derived PVDOS for all protein samples, along with the resonance Raman spectra for the oxidized samples, are compared in Figure 2. We discuss the resonance Raman data first,[70] because there is a wealth of similar spectra available for [4Fe4S] model compounds,[21,44,71] ferredoxins,[26] and HiPIPs.[26,27] The resonance Raman spectrum for D14C has also been reported previously, but in the context of a survey of five different *Pf* Fd mutants and only for the Fe–S stretching region.[12] By concentrating solely on the D14C variant, we were able to obtain better statistics in the Fe–S stretch region as well as data below 200 cm^{-1}, in the region where cluster bending and torsional modes occur.
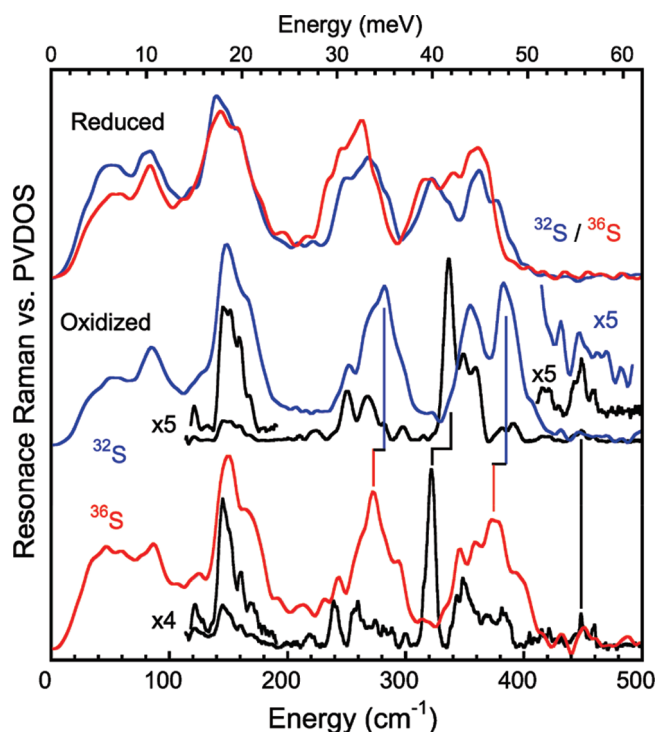
Figure 2. NRVS-derived [57]Fe PVDOS spectra and resonance Raman spectra for [57]Fe-enriched D14C Fd: (top) reduced natural abundance S (blue line) vs reduced with [36]S in bridging positions (red line), (middle) oxidized natural abundance S PVDOS (blue line) vs Raman (black line), and (bottom) oxidized, with [36]S in bridging positions, PVDOS (red line) vs Raman (black line). The resonance Raman spectra were recorded using excitation at 488 nm. A frozen buffer background spectrum has been subtracted. Vertical lines emphasize [36]S isotope shifts (or lack thereof) for some significant features.

With excitation at 488 nm, the resonance Raman spectrum of *Pf* [57]Fe D14C Fd exhibits at least nine distinct peaks in the Fe—S stretching region below 400 cm^{-1} (Figure 2) and above the ice feature at ~228 cm^{-1}. The same number of features was observed more than two decades ago with *Cp* Fd.[26] The strongest band comes from a mode at 336 cm^{-1}, compared to that at 338 cm^{-1} reported for both *Cp* Fd[26] and *Pf* D14C Fd with natural abundance Fe.[12] In D_{2d} symmetry, this mode has been labeled as a totally symmetric A_1 breathing mode, primarily Fe—S^b stretch in character.[12] Consistent with that assignment, we see a substantial (15 cm^{-1}) shift to 321 cm^{-1} with substitution of [36]S into the S^b positions. In previous work, *Cp* ferredoxin as well as model compounds exhibited 7—8 cm^{-1} shifts with [34]S substitution,[26,71] so the magnitude of the effect that we observe with [36]S is as expected.

Additional significant RR features include a pair of peaks at 348.5 and 358.5 cm^{-1}, previously taken as evidence of the descent from T_d to D_{2d} symmetry and attributed to a T_2-derived B_2/E pair that is mainly Fe—S^t in character.[12,26] Other candidate unresolved B_2/E pairs include a broad band at 381 cm^{-1} and a peak at ~250.5 cm^{-1} with an 11.5 cm^{-1} [36]S isotope shift. Finally, a band at 298 cm^{-1} has been reported in $[Fe_4S_4(SCH_2Ph)_4]^{2-}$ and *Cp* Fd spectra,[26] and we see a comparable weak peak at 297 cm^{-1}. Overall, the correspondence of features in the 250—400 cm^{-1} region between *Cp* Fd and *Pf* D14C Fd is quite remarkable, as summarized in Table 1.

Additional weak RR features can be seen above 400 cm^{-1}, with local maxima at 418 and 448 cm^{-1}. These can be assigned to

modes involving the cysteine side chains. For comparison, with $[(n\text{-Bu})_4N]_2[Fe_4S_4(SPh)_4]$, we attributed most of the motion in a 430 cm^{-1} mode to the thiophenolate ligand.[44] We also observed high-frequency cysteine ligand modes in the resonance Raman spectrum of *Pf* rubredoxin, including a band at 443 cm^{-1}.[72] For aconitase, Kilpatrick and co-workers assigned features in this region to peptide C—C—N bending modes.[29]

At low energies, additional Raman features can be discerned between (Figure 2) the ice lines at ~228 and 108 cm^{-1}. An overall low-frequency peak is seen at 146 cm^{-1}, with several apparent shoulders on the high-energy side and a lower-energy band at ~121 cm^{-1}. We note that nearly 25 years ago, Moulis and co-workers observed a RR band at ~145 cm^{-1} for *Cp* Fd.[25] The much simpler $[Fe_4S_4Cl_4]^{2-}$ complex exhibits only two peaks in this region, a strong band at 152 cm^{-1} and a weaker feature at 160 cm^{-1}. Kern et al. assigned the 152 cm^{-1} band to the A_1^{Fe} breathing mode.[35] We have found that assignment of these features is not trivial, and they are discussed following the NRVS and normal-mode analyses.

Oxidized NRVS. The [57]Fe PVDOS spectra of *Pf* D14C Fd are presented in Figure 2 (for ease of comparison, the reduced vs oxidized NRVS spectra are overlaid directly in Figure S2 of the Supporting Information). The general pattern extends a trend we have seen in Fe—S protein NRVS: as the cluster nuclearity increases, the spectra become sharper and more similar to small molecule data. This is presumably because the contribution from coupling with protein modes steadily decreases. For example, in previous rubredoxin NRVS data,[72] individual stretching modes were not well-resolved,[72] while in the *Rc* FdVI [2Fe-2S] spectra, a number of sharp Fe—S stretching modes were observed.[73] In the current [4Fe-4S] case, the Fe—S stretching regions, as well as the bending and torsional region, all exhibit well-resolved bands that return almost to baseline.

The strongest peak in the NRVS spectrum is at 148 cm^{-1} for [57]Fe D14C Fd, with additional shoulders to both sides and even a clear maximum at 84 cm^{-1}. In this low-energy region, there is reasonable conformity between the NRVS spectrum and the RR spectrum, although the RR intensity is ~1 order of magnitude weaker than in the stretching region (Figure 2). Thus, some of the most difficult to observe RR features are the easiest to observe NRVS features (and vice versa). In other ferredoxin RR spectra,[25,26] and in model compound RR studies,[21,44] low-frequency bands have been attributed to a totally symmetric A_1 Fe breathing mode. The PVDOS intensity is consistent with a large amount of Fe motion for modes in the ~148 cm^{-1} region, and the small [36]S shift suggests that the bridging sulfides move less than they do in the higher-frequency modes. More detailed interpretation of these features is deferred to the normal-mode analysis (NMA) section.

In the Fe—S stretch region, the strongest NRVS features are a broad envelope peaking near 281 cm^{-1} and twin peaks at 354 and 382 cm^{-1}. The RR features from 250 to 298 cm^{-1} align well with the NRVS envelope peaking near 281 cm^{-1}, and they point toward the rich structure that should be available with future NRVS resolution upgrades. Another cluster of RR modes overlaps nicely with the pair of high-energy NRVS peaks, although in both cases the relative intensities, as expected, vary enormously. Among the greatest contrasts between the NRVS and RR spectra is the A_1^{b} band at ~336 cm^{-1}, where there is little (but not zero) NRVS intensity. This is consistent with a mode in which most of the breathing motion is due to the bridging S, while at the same time there is very little Fe motion. Similar mismatches between
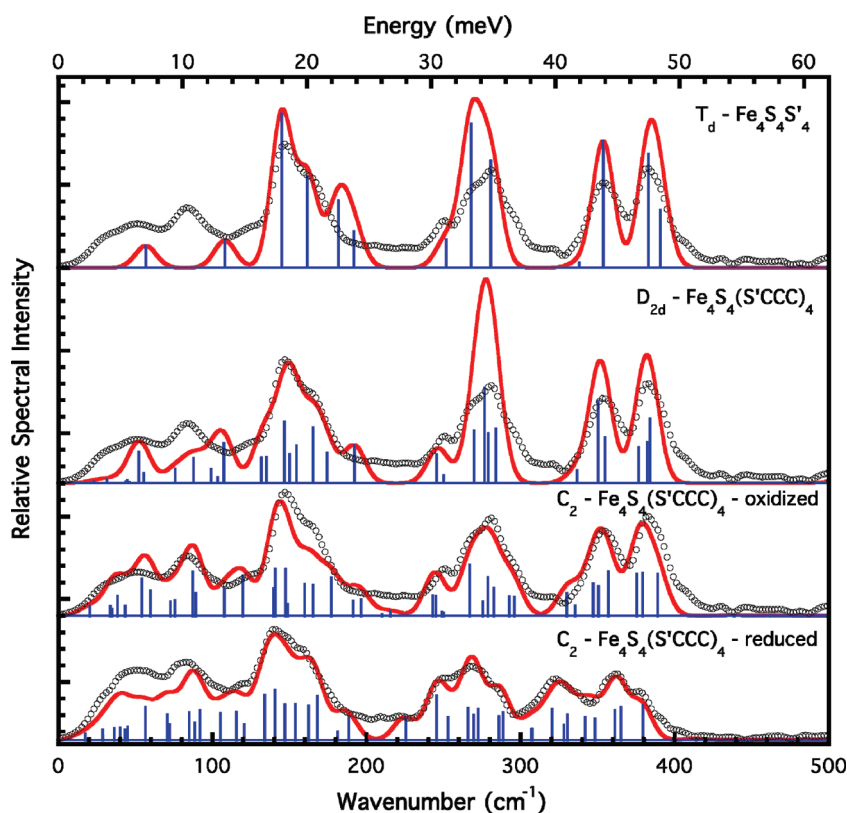
Figure 3. Urey−Bradley force field simulations (red lines) vs experimental *Pf* D14C PVDOS (○). From top to bottom: oxidized protein vs the $Fe_4S_4(S')_4$ model in T_d symmetry, the $Fe_4S_4(S'CCC)_4$ model in D_{2d} symmetry, the $Fe_4S_4(S'CCC)_4$ model in C_2 symmetry, and (d) the reduced protein vs $Fe_4S_4(S'CCC)_4$ model in C_2 symmetry. Sticks correspond to individual normal-mode frequencies and relative intensities before broadening.

NRVS and RR intensities have been observed for the FeS_4 breathing mode in rubredoxin[72] and the out-of-phase Fe_2S_6 breathing mode in 2Fe ferredoxins.[73]

The ^{57}Fe PVDOS spectra of *Pf* D14C Fd with ^{36}S in the bridging sulfide positions are also presented in Figure 2. These data show that even with its currently limited resolution, NRVS can distinguish $^{36}S-^{32}S$ isotope shifts, and these can be used for qualitative and quantitative mode assignments. In the oxidized ^{36}S sample spectrum, there are ∼13 cm^{-1} downshifts in the 281 and 382 cm^{-1} peaks to ∼268.5 and 369 cm^{-1}, respectively. Clearly, these features correspond to modes with significant bridging S motion. Again, more detailed assignments are deferred to the quantitative simulation section. In the near future, with expected resolution improvements, the less expensive ^{34}S isotope could be used for such analyses.

Reduced *Pf* D14C Fd NRVS. The ^{57}Fe PVDOS for reduced *Pf* D14C Fd with natural abundance sulfur or ^{36}S in the bridging positions are also presented in Figure 2. Because reduced $[Fe_4S_4]^+$ forms of ferredoxins have not yielded useful resonance Raman spectra to date, the current NRVS data provide the first information about the dynamics of an $[Fe_4S_4]^+$ cluster in a protein. As expected, the overall trend in the spectra for the reduced protein is for features to move to lower energies. Upon reduction, the high-frequency maximum for oxidized *Pf* D14C Fd at 382 cm^{-1} downshifts to 362 cm^{-1}, and the middle band at 281 cm^{-1} moves to 268.5 cm^{-1}. We note that band shifts that are comparable in magnitude have been observed for electronic changes in the opposite direction. For example, oxidation of HiPIP proteins from the $[Fe_4S_4]^{2+}$ to the $[Fe_4S_4]^{3+}$ redox level upshifts many of the

Fe−S stretching modes by ∼20 cm^{-1}.[27] In both cases, the ∼5% shifts are much smaller than the ∼17% shift seen in rubredoxin stretching frequencies upon reduction.[72] This is qualitatively what one would expect if the additional electron in the ferredoxin case were relatively delocalized over the $[Fe_4S_4]^+$ cluster. Because redox changes in either direction are accompanied by changes in structure and symmetry, there is not necessarily a 1:1 correspondence between normal modes in different redox levels, and a more detailed analysis of redox shifts (and ^{36}S isotope shifts) requires quantitative normal-mode analysis.

Empirical Force Field Normal-Mode Analysis. Comparisons between the experimentally derived PVDOS $[D_{Fe}(\bar{v})]$ for oxidized and reduced *Pf* D14C Fd and a sequence of $D_{Fe}(\bar{v})$ curves calculated from an empirical Urey−Bradley force field are shown in Figure 3. A more extensive set of simulations, as well as those for the ^{36}S isotopomers, which were part of the refinement, is included as Supporting Information.

As with previous rubredoxin[72] and $[2Fe-2S]$ ferredoxin[73] NRVS studies, we began with small, high-symmetry models, and we then progressively both increased the model size and lowered the symmetry until reasonable agreement was obtained. Resonance Raman spectra of $[Fe_4S_4]$ ferredoxins,[25,26] aconitase,[29] and $[Fe_4S_4(SR)_4]^{n-}$ model complexes[21,25,26,44] have been interpreted with such empirical force fields, and our analysis again relies on much of this body of work. For the high-symmetry models in which RR modes could be unambiguously assigned, these data were also included in the optimization procedure. The calculated frequencies and ^{36}S isotope shifts for the high-frequency normal modes of these simple models are compared
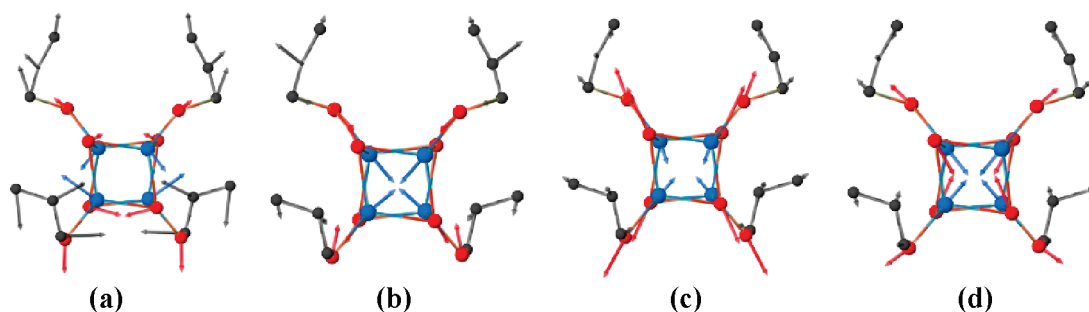
Figure 4. A symmetry normal modes calculated from the C_2 UBFF (calculated frequencies): (a) 87, (b) 177, (c) 336, and (d) 389 cm^{-1}. The conventional atomic coloring scheme has been modified for the sake of clarity: black for C, blue for Fe, and red for S.

with the experimental data for oxidized Fd in Table 1, while the resulting parameters are summarized in the Supporting Information.

T_d Fe$_4$S$_4$(S′)$_4$ and D_{2d} Fe$_4$S$_4$(S′CCC)$_4$ Models. The simplest model that has been used to explain the dynamics of ferredoxin redox sites is an Fe$_4$S$_4$(S′)$_4$ model in T_d symmetry, analogous to the [Fe$_4$S$_4$Cl$_4$]$^{2-}$ simulation (Figure 1). We started with this model and adjusted the Urey−Bradley force field parameters to match the main peaks in the experimental $D_{Fe}(\bar{\nu})$ spectrum. As shown in Figure 3, such a tetrahedral model correctly reproduces all of the major features of the PVDOS. However, in the case of the protein, the predicted PVDOS features from the simple model are too sharp and consequently too intense (because the total area must be constant). Broadening can be achieved by having more bands, either by splitting degeneracies at lower symmetries or through a larger model with more atoms. We thus lowered the symmetry to D_{2d}, to allow for the well-known distortion of the [4Fe-4S] core, and also added one, two, or three carbons to each side chain in the model, to allow for the often discussed coupling of Fe−S motion with S−C−C bending.[70] We also added major RR-mode frequencies as additional constraints. As illustrated for the D_{2d} Fe$_4$S$_4$(S′CCC)$_4$ simulation in Figure 3, this extra freedom produced significant improvement in the bending region near 150 cm^{-1}, but it yielded only modest improvement in the stretching region above 200 cm^{-1}. We thus explored a different symmetry.

C_2 Fe$_4$S$_4$(S′CCC)$_4$ Model. Although model compound [4Fe-4S] cores often have exact or approximate D_{2d} symmetry,[4] in proteins the additional cysteine side chains are often better described by C_2 symmetry. In fact, in the structure of the nitrogenase Fe protein, the cluster lies on the protein dimer 2-fold axis.[74] C_2 symmetry was also used to describe the cluster in the low-temperature form of (Bu$_4$N)$_2$[Fe$_4$S$_4$(SPh)$_4$].[75] Because the importance of coupling with cysteine side chain motion is well-documented, we proceeded to refine an Fe$_4$S$_4$(SCCC)$_4$ model with a D_{2d} core and with the side chains in C_2 symmetry. As shown in Figure 3, the calculated normal modes for this model are in much better agreement with the stretching region of the NRVS PVDOS, and this model also provides a better fit to the features between 50 and 100 cm^{-1}. For the sake of completeness, we also examined models that used the exact crystal structure and complete cysteine residues. There was additional modest improvement, which is included in the Supporting Information.

Reduced *Pf* D14C Fd Simulations. We obtained similar results when simulating the NRVS spectrum of the reduced D14C ferredoxin, except that many bands were downshifted by ∼5% (Figure 3 and the Supporting Information). With the simplest comparison, using T_d symmetry and an unchanged

cluster structure, we obtained a 10% reduction in $K(\text{Fe−S}^b)$, the stretching force constant for the distance from Fe to the bridging sulfides changing from 0.93 to 0.84 mdyn/Å (Supporting Information). A larger 22% reduction, from 1.28 to 1.0 mdyn/Å, was observed for $K(\text{Fe−S}^t)$, the stretching force constant for the distance from Fe to the terminal thiolate sulfurs. However, in the more exact C_2 model with the D_{2d} core, $K(\text{Fe−S}^t)$ is reduced by 5 and 7% in the hypothetical reduced cluster model and unaltered structure, respectively. We observed a 13% reduction in longer Fe−S^b bonds while keeping the shorter Fe−S^b force constant unchanged in the reduced cluster. However, $K(\text{Fe−S}^b)$ for long and short Fe−S^b bonds experiences 4 and 5% reductions, respectively, when the same cluster is retained.

Illustration of Normal Modes. We close the Urey−Bradley assignments by illustrating modes that are significant in either the resonance Raman or NRVS PVDOS. In particular, we illustrate (all modes are "A" symmetry) (a) an ∼87 cm^{-1} shearing mode that contributes intensity in the low-energy region, (b) the ∼177 cm^{-1} breathing mode that skews the intensity of the strongest NRVS peak, (c) the ∼336 cm^{-1} mode responsible for the strongest resonance Raman feature, and (d) the ∼389 cm^{-1} Fe−S^t mode responsible for the highest-frequency (main spectrum) resonance Raman feature. The eigenvectors derived from the UBFF model are illustrated in Figure 4.

Full Protein CHARMM Calculations. The degree of coupling between the local motions of Fe−S centers and the protein matrix has been the subject of considerable discussion and investigation.[42,43,76−78] It is also an issue with relevance for electron transfer, conformational switching, and even "magnetostructural"[79] properties of these sites. We investigated this coupling via full protein normal-mode calculations, using a supplemented CHARMM force field[62] guided by the previous Urey−Bradley calculations and the Fe PVDOS. The results are compared with the experimental data in Figure 5. As shown in Figure 5, the PVDOS for *Pf* D14C Fd retains relatively sharp structure down to ∼80 cm^{-1}, whereas the PVDOS for the Rc6 [2Fe-2S] Fd has relatively broad features commencing around 300 cm^{-1}.[73] With the full protein calculation, we see that the sharp structure arises from a small number of relatively intense modes. The degree of localization of these modes can be quantified using a collectivity calculation, in which a lower collectivity indicates a smaller number of atoms contributing to the mode.[63,64] In the Fe−S stretching region, the mode that presumably corresponds to the RR band at 336 cm^{-1} has a low collectivity of 0.05, implying 0.05 × 430 (∼21) atoms, or effectively the [4Fe-4S] core cluster and not much more than the SCC ligands. Many of the strong NRVS modes have
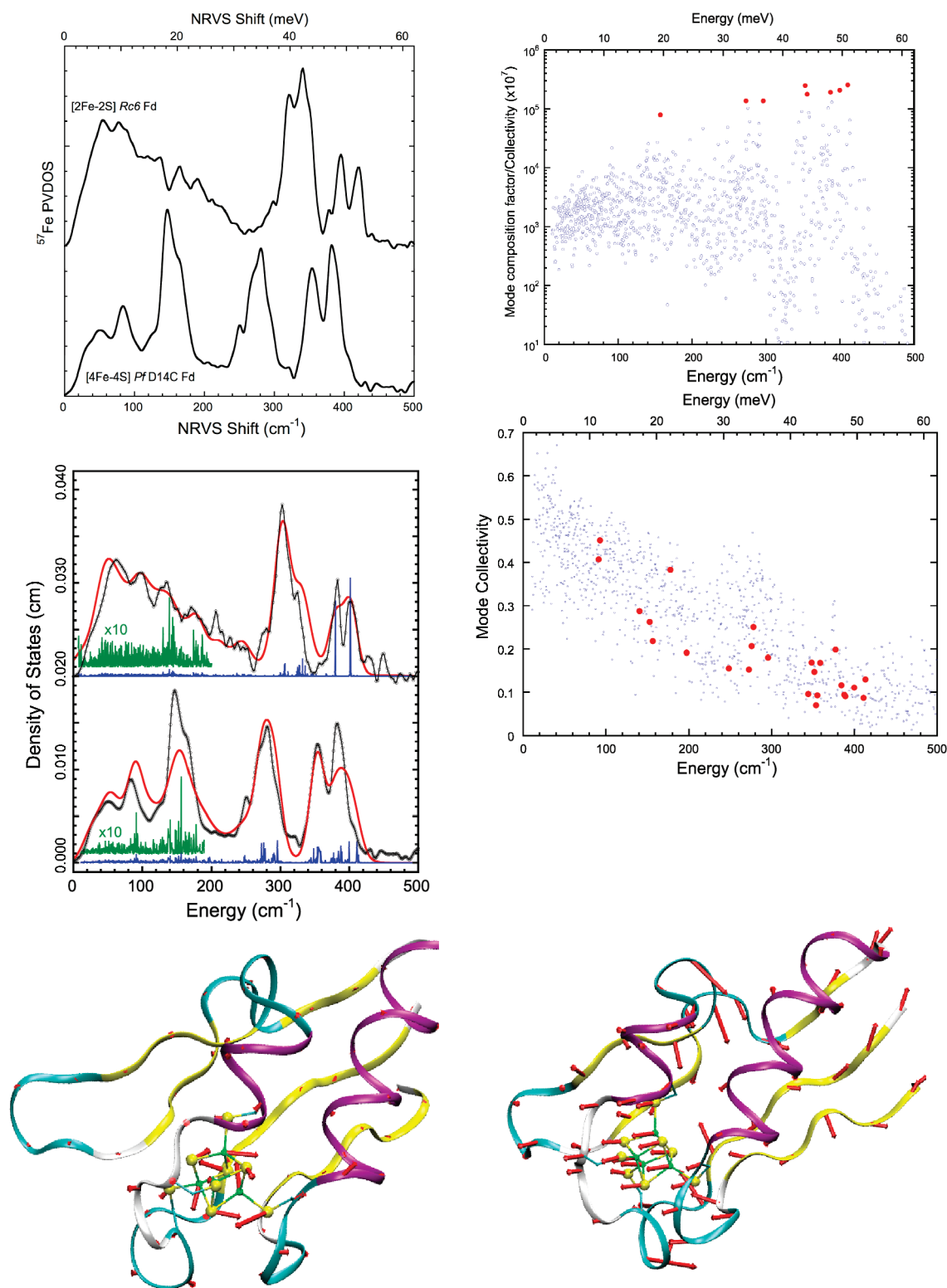
Figure 5. Full protein calculation analysis of oxidized *Pf* D14C Fd. Experimental PVDOS (black lines) of oxidized Rc6 Fd and oxidized *Pf* D14C Fd (top left). Experimental PVDOS (black lines) vs calculated spectra (red lines) for reduced Rc6 Fd and oxidized *Pf* D14C Fd (middle left). Sticks represent the mode composition factors of individual modes. Degree of collectivity for normal modes with largest mode composition factors highlighted in red (bottom) and mode composition factor divided by the degree of collectivity to emphasize cluster-centered normal modes (top) (two top right panels). The bottom panels are illustrations of calculated normal modes at (left) 157 cm^{-1} and (right) 16 cm^{-1}.

collectivity on the order of 0.07−0.10 atom, implying that 30−43 atoms contribute most of the mode's motion. This in turn would represent each of the cysteine residues and perhaps one additional amino acid.
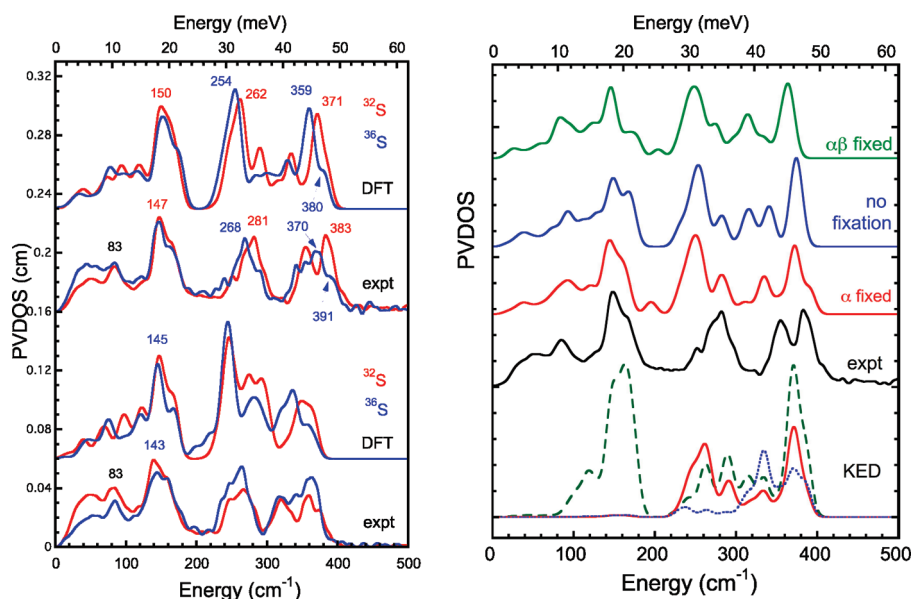
Figure 6. DFT simulations and experimental data (left) for natural abundance (red lines) and ^{36}S-substituted Fd (blue lines), comparing predicted and observed isotope shifts for substitution of ^{36}S into bridging positions for the oxidized (top) and reduced (bottom) samples. DFT using GAUSSIAN and different geometry optimization approaches (top right). From top to bottom: D14C oxidized DFT without side chain relaxation (α- and β-carbons of Cys fixed), DFT with both α- and β-carbons relaxed, DFT with α-carbons fixed to their X-ray positions and β-carbons relaxed, and experiment. DFT-calculated kinetic energy distributions (KED) (bottom right) for *Pf* D14C Fd models, showing relative contributions from Fe−S^b (green line), Fe−S^t (blue line), and Fe−Fe (red line) stretching.

The Fe-centered modes can be accentuated by plotting R_{ek}, the ratio of "mode composition factor" e_{Fe}^2 to collectivity κ. To put these values in context, we compare the peak values of this ratio for D14C with previous results for the Rc6 [2Fe-2S] ferredoxin, over the range from 100 to 400 cm^{-1}. This allows us to quantify the qualitative impression from the PVDOS that the localized modes extend to lower frequencies in the [4Fe-4S] cluster. In the 100−300 cm^{-1} region, values of R_{ek} as high as 0.01 are observed, whereas for Rc6 ferredoxin, the highest values are more than 3-fold lower. Thus, compared to the [2Fe-2S] cluster, over most of the spectrum the [4Fe-4S] cluster is a more dynamically isolated unit. This can be seen for the CHARMM calculation of a mode at 157 cm^{-1}, which exhibits breathing of the cluster with relatively little protein motion (Figure 5).

The CHARMM calculations are also useful for characterizing the very low-frequency modes, where the protein movements are highly collective, containing a large amount of coherent [4Fe-4S] cluster motion. An example is the lowest-frequency mode at 16 cm^{-1} (Figure 5), which exhibits concerted motion of the [4Fe-4S] cluster and nearby polypeptide in one direction, while the far end of the protein moves in the opposite direction. Again, we postpone discussion of potential consequences of such modes to the final part of this paper.

***Pf* D14C Fd DFT Analysis.** The power of DFT calculations for interpretation of [4Fe-4S] cluster dynamics has already been illustrated with the $[Fe_4S_4Cl_4]^{2-}$ calculations in Figure 1, as well as our previous analysis of the $[^{57}Fe_4S_4(SC_6H_5)_4]^{2-}$ ion.[44] For a theoretical simulation of the D14C spectra, we used a $[^{57}Fe_4S_4(SCH_2CH_3)_4]^{2-}$ model, and a comparison of the DFT-calculated PVDOS with the experimental data is given in Figure 6. Throughout the following discussion, we refer to peak positions of experimental and DFT values for the oxidized form. The best agreement was found for the bending- and breathing-mode region from 100 to 200 cm^{-1}, where the DFT matches the

shape and intensity of the major PVDOS feature at ∼147/150 cm^{-1} (Experimental/DFT values here and below), while at lower frequencies, there is a minor discrepancy in the low-energy 83/92 cm^{-1} peak. As with the $[Fe_4S_4Cl_4]^{2-}$ analysis (Figure 1), the predicted frequencies in the Fe−S stretch region are generally underestimated by 2−7%. Overall, the relative intensities and shape of the experimental peaks are reasonably well reproduced by DFT.

The accuracy of the ^{36}S isotope shifts by DFT reflects how well the calculations estimate the amount of motion of the four labeled bridging S atoms in a particular mode. As illustrated in Figure 6, the DFT predictions for the shifts in the PVDOS with ^{36}S^b substitution agree quite well with the observed data. In particular, a strong band at 383/371 cm^{-1} shifts to 370/359 cm^{-1} with ^{36}S, allowing a less-shifted high-frequency peak at 391/380 cm^{-1} to be resolved. The DFT-predicted 12 cm^{-1} (from 371 to 359 cm^{-1}) shift is in accordance with the observed 13 cm^{-1} (from 383 to 370 cm^{-1}) value.

To better illustrate the nature of the normal modes predicted by DFT calculations, in Figure 6, we also display results from a kinetic energy decomposition (KED) approach, where the composition of the forces involved has been decomposed into Fe−S^b, Fe−S^t, and Fe−Fe contributions. (The Fe−Fe contribution is redundant with bending of internal cube angles.[26]) For the most part, the DFT analysis confirms what has been surmised from years of empirical simulations. (1) Modes below 200 cm^{-1} are almost all Fe−S^b stretch (the major peak at 147/150 cm^{-1}). (2) Modes between 200 and 300 cm^{-1} are mostly bending, or Fe−Fe stretch (with the major peak at 281/262 cm^{-1}). (3) Modes between 300 and 400 cm^{-1} are highly mixed (with the major peak at 383/371 cm^{-1}). Notably, the integral intensities of the KED profiles are normalized to the number of stretching bonds, namely, to 12 for Fe−S^b bonds, 4 for Fe−S^t bonds, and six for Fe−Fe contributions.

Role of the Protein Matrix Restraint and Size of the Cysteinyl Ligand Model. The role of the protein matrix in restraining the Fe−S cluster motion and thereby influencing NRVS spectra can be estimated, in the first approximation, via different schemes for fixing the cysteinyl side chain conformations of our $[Fe_4S_4(SCH_2CH_3)_4]^{2-}$ model (see Methods). This type of examination is also useful for finding an appropriate DFT modeling approach for NRVS spectra. Notably, the results reported in the left panel of Figure 6 were obtained using an "intermediate" fixation level where only the four terminal ethyl thiolate carbons modeling α-carbons of the cysteinyls were restrained to their initial crystallographic positions (α- and β-carbon positions are labeled as $^-SC_\beta H_2 C_\alpha H_3$ in our cysteinyl model). When completely releasing constraints or restraining both β- and α-carbons to their initial positions, we obtained somewhat different NRVS spectra, as shown in the right panel of Figure 6. Examination of simulated NRVS spectra resulting from the three fixation approaches suggests that the intermediate fixation scheme provides the best correspondence with the experiment.

Inner-Sphere Reorganization Energy of the [4Fe-4S] Cluster. Given the function of the Pf Fd [4Fe-4S] cluster in electron transport, we examined this functionality using our DFT models. The reorganization energy λ, which is the energy of the structural relaxation following electron transfer, can be predicted from the DFT calculations. Once λ is known, then according to Marcus theory,[80] the activation barrier for electron transfer $(\Delta G^\ddagger)$ is predicted to depend on λ and the driving force ΔG^o by the relationship $\Delta G^\ddagger = (\lambda + \Delta G^\circ)^2/4\lambda$, and the rate of electron transfer is then given by

$$k_{ET} = \frac{2\pi}{\hbar} \frac{T_{DA}^2}{\sqrt{4\pi\lambda k_B T}} \exp\left(\frac{-\Delta G^\ddagger}{4 k_B T}\right)$$

where T_{DA} is the term for electronic coupling between the two sites.

Previous theoretical assessments of Fe−S cluster reorganization energies focused on λ_i, the contribution from the inner-sphere structural features, which consist of the Fe sites and their first coordination spheres.[69] The other component, the outer-sphere reorganization energy λ_o, reflects the contribution from the surrounding protein and the solvent. For our analysis, the complete system of the calculation (the four Fe sites and their first-shell ligands, namely, four bridging S and four Cys ligands) represents the inner-sphere structure. Using procedures described in Methods, we obtained a value of 18.8 kJ/mol for λ_i.

Our value for the inner-sphere reorganization energy of the oxidized Pf D14C Fd [4Fe-4S] cluster is smaller than the values previously reported for [4Fe-4S] models, which to the best of our knowledge range between ∼30 and ∼50 kJ/mol.[69,81] Our modeling is different from the preceding studies in two structural aspects. First, we used larger ethyl thiolate ($CH_3CH_2S^-$) models for Cys side chains, as compared to methyl thiolates in previous studies. Second, we fixed the positions applied at the α-carbons, as compared to completely relaxed geometry optimizations. Our relatively small values can be compared to early experimental estimates of a combined value of 32 kJ/mol for the inner-sphere part of λ in self-exchange for the [4Fe-4S] model complexes,[82] as well as a recent CHARMM calculation that gave a total λ of 18 kJ/mol for electron transfer in *Clostridium acidurici* ferredoxin.[83]

DISCUSSION

In this work, we have extracted the ^{57}Fe PVDOS of the [4Fe-4S] cluster in Pf D14C Fd through the NRVS technique. The results have been compared with resonance Raman data and simulated using CHARMM and DFT calculations. In addition, for the first time, we have examined the PVDOS for a reduced [4Fe-4S] cluster. In both cases, additional information was obtained from ^{36}S substitution of the bridging sulfide positions.

One strength of the NRVS method is the facile computation of the resulting PVDOS spectra. This is illustrated in the results for the simple model cluster, $[Fe_4S_4Cl_4]^{2-}$. Whereas in the past force fields for this molecule have been derived from RR frequencies above 230 cm^{-1}, our empirical force field has the additional constraint of NRVS amplitudes, as well as a range of additional modes extending to less than 100 cm^{-1}. With a modest adjustment of previous empirical force fields, we were able to almost exactly model the Fe−S and Fe−Cl stretching-mode spectrum from 400 to ∼240 cm^{-1}. However, in the bending and torsion range from 200 to 50 cm^{-1}, the DFT calculations were better at reproducing the strength and order of these "softer" motions.

Turning to the Pf D14C Fd spectrum, we observed the same basic pattern, but complicated by the coupling with cysteine side chains and the protein matrix. Correct modeling of the PVDOS spectrum required inclusion of correct Fe−S−C−C dihedral angles. As shown years ago by Spiro and co-workers,[42] the degree of coupling between Fe−S stretch and S−C−C bend motions is dependent on the Fe−S−C−C dihedral angle, with maximal coupling when the atoms are coplanar and the angle is 0° or 180°. In the case of Pf D14C Fd, crystallography shows that the average dihedral angle is within 19° of 90°; hence, the Fe−S motion is relatively independent of S−C−C bending. The specific effects on [4Fe-4S] clusters were discussed by Backes et al.,[27] who noted that Fe−S−C−C dihedral angles near 90° were conserved across a number of [4Fe-4S] ferredoxins, whereas rubredoxins, [2Fe-2S] ferredoxins, and HiPIPs tended to have at least one Fe−S−C−C angle near 180°. Another factor that presumably contributes to this isolation is simple connectivity; only one of four Fe ligands is directly coupled to the protein, compared to two of four in the [2Fe-2S] ferredoxins and four of four in rubredoxins. Overall, compared to those of the [2Fe-2S] ferredoxins, the normal modes of the [4Fe-4S] cluster were more dynamically isolated from the protein. This isolation can be quantified by full protein normal-mode calculations using a supplemented CHARMM force field.

Because the normal modes constitute a complete basis set, one implication of Fe-centered modes is that changes in the [4Fe-4S] cluster geometry are relatively decoupled from the protein matrix. Thus, the inevitable structural rearrangements during redox have little effect on the protein. In Marcus theory, the energetics of these distortions are usually broken into inner- and outer-sphere reorganization energies. As a complement to the Urey−Bradley and CHARMM calculations, we have used DFT calculations to simulate the PVDOS spectra and also to estimate the reorganization energy (λ_i) of the [4Fe-4S]$^{2+}$ to [4Fe-4S]$^+$ transition. The estimated λ_i of 19 kJ/mol is significantly lower than the values of ∼27−37 kJ/mol previously estimated for a [2Fe-2S] Fd model system or the value of ∼29 kJ/mol obtained for reduction of a [4Fe-4S]$^{2+}$ Fd model system. These results would suggest that, for transport between nearly equivalent clusters, where the driving force $\Delta G^\circ \sim 0$, electron transfer will

proceed more quickly between [4Fe-4S] clusters than between [2Fe-2S] clusters.

Having now examined both [2Fe-2S] and [4Fe-4S] systems by NRVS and calculations, we may address a long-standing question of why nature "chooses" one cluster over another for electron transport functions. As noted by Meyer, it is "difficult to rationalize on biochemical grounds why the [4Fe-4S] folds should outnumber the [2Fe-2S] ones by more than a factor of 4".[7] For some, "the choice of the type of iron—sulfur cluster (i.e., the number of iron ions and the type of ligands) seems to be mainly a question of stability and oxidation potential[69]". Nevertheless, there is considerable overlap in the range of available redox potentials for [2Fe-2S] clusters (from −230 to −460 mV) and [4Fe-4S] clusters (from 0 to −645 mV).

The dynamical isolation and low reorganization energies of [4Fe-4S] clusters might be a factor in nature's "choice" of which clusters to use in electron transfer processes. If other factors are equal, for transport over long distances, [4Fe-4S] clusters would seem to yield the most rapid electron transport. This may explain their use in long electron transport chains such as the *E. coli* nitrate reductase NarH subunit, where four [4Fe-4S] clusters are arranged at 12−14 Å intervals,[84] or in complex I, which possesses a chain of five [4Fe-4S] clusters (along with four other Fe−S clusters) at 12−17 Å intervals.[85]

In other cases, an enzyme might need to couple electron transfer with a conformational change to favor dissociation of redox partners. For example, the [2Fe-2S] ferredoxin known as putidaredoxin (Pdx) shows a redox-dependent affinity for its physiological partner, cytochrome P-450$_{cam}$, with a 100-fold decrease in the binding constant upon transfer of an electron from the reduced [2Fe-2S]$^+$ cluster to the P-450 heme site.[86] This helps avoid product inhibition in the electron transfer process. In the other redox direction, for the [2Fe-2S] adrenodoxin (Adx) interacting with adrenodoxin reductase (AdR), the binding constant for the AdR−Adx complex decreases by a factor of 20 upon reduction of the Fe−S center, thus promoting the dissociation of the reduced Adx from AdR. Similarly, in photosynthesis, redox-linked conformational changes of a [2Fe-2S] ferredoxin are implicated in the disassembly of the Fd−FNR complex after cluster oxidation[87] and presumably occur in the opposite direction upon reduction of Fd by photosystem I. One could thus argue that when a process benefits from a conformational change with redox activity, the greater bond length changes and the tighter coupling of a [2Fe-2S] cluster with the protein matrix become a benefit instead of a liability. Of course, the driving force for these conformational changes will be a mix of factors, including electrostatics, van der Waals interactions, and hydrogen bonding as well as these quasi-mechanical factors. On occasion, the need for conformational control might outweigh the benefits of fast electron transfer. In the particular case of *Pf* Fd, we note that the native protein has an aspartate ligand to the [4Fe-4S] cluster. NMR work by Calzolai et al.[88] indicated a >5000-fold slower self-exchange rate for native versus D14C at 10 °C; as expected for λ, the reorganization energy increased by 19 kcal/mol. In this case, a localized "carboxylate shift" at Asp during cluster redox was proposed to play a role in gating electron transfer.[88]

SUMMARY AND CONCLUSIONS

In this study, the combined application of ^{57}Fe NRVS and resonance Raman spectroscopy with empirical and DFT modeling has provided a broader view of [4Fe-4S] cluster dynamics in oxidized and reduced forms of an electron transfer protein. In the 100−200 cm^{-1} bending and breathing region, we found surprisingly good correspondence between the NRVS and RR spectra, while in the Fe−S stretching region from 250 to 400 cm^{-1}, the two approaches agreed on frequencies but contrasted sharply in intensity. Despite the relatively localized nature of [4Fe-4S] cluster normal modes, we found that the quantitative reproduction of the NRVS spectrum depended on the correct description of cysteine side chain conformations.

Unambiguous signals were seen in the NRVS spectrum from ∼50 to >400 cm^{-1}. An ∼84 cm^{-1} mode was found to involve a shearing motion of the cluster combined with a large amount of concerted side chain motion. Such low-frequency modes, have not previously been seen in [4Fe-4S] ferredoxins, and spectra in this region might serve as diagnostics of conformational change. Overall, the strongest features in the ferredoxin NRVS spectrum were asymmetric peaks at ∼148 cm^{-1}, with higher-energy shoulders at ∼161 cm^{-1}. This region was found to include symmetric and asymmetric Fe$_4$ breathing modes for the cluster, and the detailed structure was profoundly sensitive to local conformation via coupling with the cysteine side chains. At higher frequencies, in the Fe−S stretching region, NRVS provided the first information about the vibrational dynamics of a reduced [Fe$_4$S$_4$]$^+$ cluster, which has not been accessible by resonance Raman spectroscopy. Reduction caused downshifts of band centroids of ∼4.7−7.3%. In empirical simulations, we found that the Fe−S stretching force constant for terminal thiolates and bridging sulfides decreased by ∼16 and ∼9%, respectively. The reduction is 5−7% for Fe-terminal thiolate stretches and 0−13% for Fe-bridging sulfide stretches, depending on whether we retained same cluster or used reduced hypothetical cluster structures.

NRVS provides an information-rich spectroscopy for biological systems containing ^{57}Fe and dozens of other isotopes. Although the current data were taken at ∼9−10 cm^{-1} resolution, monochromators with resolution down to ∼1 cm^{-1} can be and have been made.[89,90] Of course, resolution without flux does not yield a viable experiment, but future synchrotron radiation sources could provide spectral brightness greater by orders of magnitude.[91,92] With better sources, a variety of imaging and time-dependent NRVS experiments would become feasible, and nuclear spectroscopy could serve a much broader community of chemical and biological scientists.

■ ASSOCIATED CONTENT

ⓢ Supporting Information. Table of force constants used, table of assignments for ^{36}S spectra, Mössbauer spectra of oxidized and reduced samples, and additional NRVS simulations of alternate structures and ^{36}S isotopomers. This material is available free of charge via the Internet at http://pubs.acs.org.

■ AUTHOR INFORMATION

Corresponding Author
*Telephone: (530) 752-0360. Fax: (530) 752-2444. E-mail: spjcramer@ucdavis.edu.

■ ACKNOWLEDGMENT

■ ABBREVIATIONS

NRVS, nuclear resonance vibrational spectroscopy; RR, resonance Raman; IR, infrared; EPR, electron paramagnetic resonance; DFT, density functional theory; UB, Urey—Bradley; FF, force field; PVDOS, partial vibrational density of states; *Pf*, *P. furiosus*; Fd, ferredoxin; NMA, normal-mode analysis; HiPIP, high-potential iron protein; PDB, Protein Data Bank; *Cp*, *C. pasteurianum*; *Ca*, *C. acidi-urici*; fwhm, full width at half-maximum; KED, kinetic energy decomposition.

■ REFERENCES

(1) Wachtershauser, G. (2007)On the chemistry and evolution of the pioneer organism. *Chem. Biodivers. 4*, 584–602.

(2) Lill, R., and Muhlenhoff, U. (2008)Maturation of iron-sulfur proteins in eukaryotes: Mechanisms, connected processes, and diseases. *Annu. Rev. Biochem. 77*, 669–700.

(3) Mortenson, L. E., Valentine, R. C., and Carnahan, J. E. (1962)An Electron Transport Factor from *Clostridium pasteurianum*. *Biochem. Biophys. Res. Commun. 7*, 448–452.

(4) Beinert, H., Holm, R. H., and Münck, E. (1997)Iron-Sulfur clusters: Nature's modular, multipurpose structures. *Science 277*, 653–659.

(5) Bian, S., and Cowan, J. A. (1999)Protein-bound iron—sulfur centers. Form, function, and assembly. *Coord. Chem. Rev. 190—192*, 1049–1066.

(6) Johnson, D. C., Dean, D. R., Smith, A. D., and Johnson, M. K. (2005)Structure, function, and formation of biological iron-sulfur clusters. *Annu. Rev. Biochem. 74*, 247–281.

(7) Meyer, J. (2008)Iron-sulfur protein folds, iron-sulfur chemistry, and evolution. *J. Biol. Inorg. Chem. 13*, 157–170.

(8) Adams, M. W. W. (1994)Biochemical diversity among sulfur-dependent, hyperthermophilic microorganisms. *FEMS Microbiol. Rev. 15*, 261–277.

(9) Kim, C., Brereton, P. S., Verhagen, M., and Adams, M. W. W. (2001) Ferredoxin from *Pyrococcus furiosus*. In *Hyperthermophilic Enzymes*, Part C, pp 30—40, Academic Press Inc., San Diego.

(10) Zhou, Z. H., and Adams, M. W. W. (1997)Site-directed mutations of the 4Fe-ferredoxin from the hyperthermophilic archaeon *Pyrococcus furiosus*: Role of the cluster-coordinating aspartate in physiological electron transfer reactions. *Biochemistry 36*, 10892–10900.

(11) Brereton, P. S., Verhagen, M. F. J. M., Zhou, Z. H., and Adams, M. W. W. (1998)Effect of Iron-Sulfur Cluster Environment in Modulating the Thermodynamic Properties and Biological Function of Ferredoxin from *Pyrococcus furiosus*. *Biochemistry 37*, 7351–7362.

(12) Brereton, P. S., Duderstadt, R. E., Staples, C. R., Johnson, M. K., and Adams, M. W. W. (1999)Effect of Serinate Ligation at Each of the Iron Sites of the [Fe4S4] Cluster of *Pyrococcus furiosus* Ferredoxin on the Redox, Spectroscopic, and Biological Properties. *Biochemistry 38*, 10594–10605.

(13) Torres, R. A., Lovell, T., Noodleman, L., and Case, D. A. (2003) Density Functional and Reduction Potential Calculations of Fe4S4 Clusters. *J. Am. Chem. Soc. 125*, 1923–1936.

(14) Jensen, K. P., Ooi, B.-L., and Christensen, H. E. M. (2007) Accurate Computation of Reduction Potentials of 4Fe-4S Clusters Indicates a Carboxylate Shift in *Pyrococcus furiosus* Ferredoxin. *Inorg. Chem. 46*, 8710–8716.

(15) Dey, A., Jenney, F. E. J., Adams, M. W., Babini, E., Takahashi, Y., Fukuyama, K., Hodgson, K. O., Hedman, B., and Solomon, E. I. (2007) Solvent tuning of electrochemical potentials in the active sites of HiPIP versus ferredoxin. *Science 318*, 1464–1468.

(16) Johannessen, M. N., Nielsen, M. S., Ooi, B. L., Christensen, H. E. M., and Harris, P. (2007) The crystal structure of the all cysteinyl coordinated D14C variant of [4Fe-4S] *Pyrococcus furiosus* ferredoxin. Protein Data Bank entry 2Z8Q.

(17) Humphrey, W., Dalke, A., and Schulten, K. (1996)VMD: Visual Molecular Dynamics. *J. Mol. Graphics 14*, 33–38.

(18) Rao, P. V., and Holm, R. H. (2004)Synthetic Analogues of the Active Sites of Iron-Sulfur Proteins. *Chem. Rev. 104*, 527–559.

(19) Fee, J. A., Castagnetto, J. M., Case, D. A., Noodleman, L., Stout, C. D., and Torres, R. A. (2003)The circumsphere as a tool to assess distortion in [4Fe-4S] atom clusters. *J. Biol. Inorg. Chem. 8*, 519–526.

(20) Hagen, K. S., and Uddin, M. (2008)A Continuous Symmetry Measure of [4Fe-4S]$^+$ Core Distortions and Analysis of Supramolecular Synthons in Crystal Structures of $(Et_4N)_3[Fe_4S_4Cl_4] \cdot Et_4NCl$ at 100 and 295 K. *Inorg. Chem. 47*, 11807–11815.

(21) Kern, A., Nather, C., Studt, F., and Tuczek, F. (2004)Application of a Universal Force Field to Mixed Fe/Mo-S/Se Cubane and Heterocubane Clusters. 1. Substitution of Sulfur by Selenium in the Series $[Fe_4X_4(YCH_3)_4]^{2-}$; X = S/Se and Y = S/Se. *Inorg. Chem. 43*, 5003–5010.

(22) Noodleman, L., and Case, D. A. (1992)Density-Functional Theory of Spin Polarization and Spin Coupling in Iron-Sulfur Clusters. *Adv. Inorg. Chem. 38*, 423–470.

(23) Segal, B. M., Hoveyda, H. R., and Holm, R. H. (1998)Terminal Ligand Assignments Based on Trends in Metal—Ligand Bond Lengths of Cubane-Type $[Fe4S4]^{2+,+}$ Clusters. *Inorg. Chem. 37*, 3440–3443.

(24) Williams, J. B., and Köckerling, M. (2001)Synthesis and structure of an unprecedented high-symmetry $[Fe_4S_4Cl_4]$ cubane-type unit in supramolecular $[K_4(FeCl_4)(C_{12}H_{24}O_6)_4][Fe_4S_4Cl_4]$. *Chem. Commun.*, 1380–1381.

(25) Moulis, J.-M., Meyer, J., and Lutz, M. (1984)$[4Fe-4S]^{2+}$ (X = Sulfur, Selenium) Clusters in *Clostridium pasteurianum* Ferredoxin and in Synthetic Analogues: Structural Data from Resonance Raman Spectroscopy. *Biochemistry 23*, 6605–6613.

(26) Czernuszewicz, R. S., Macor, K. A., Johnson, M. K., Gewirth, A., and Spiro, T. G. (1987)Vibrational Mode Structure and Symmetry in Proteins and Analogues Containing Fe4S4 Clusters: Resonance Raman Evidence for Different Degrees of Distortion in HiPIP and Ferredoxin. *J. Am. Chem. Soc. 109*, 7178–7187.

(27) Backes, G., Mino, Y., Loehr, T. M., Meyer, T. E., Cusanovich, M. A., Sweeney, W. V., Adman, E. T., and Sanders-Loehr, J. (1991)The Environment of Fe4S4 Clusters in Ferredoxins and High-Potential Iron Proteins. New Information from X-ray Crystallography and Resonance Raman Spectroscopy. *J. Am. Chem. Soc. 113*, 2055–2064.

(28) Conover, R. C., Kowal, A. T., Fu, W. G., Park, J. B., Aono, S., Adams, M. W., and Johnson, M. K. (1990)Spectroscopic characterization of the novel iron-sulfur cluster in *Pyrococcus furiosus* ferredoxin. *J. Biol. Chem. 265*, 8533–8541.

(29) Kilpatrick, L. K., Kennedy, M. C., Beinert, H., Czernuszewicz, R. S., Qiu, D., and Spiro, T. G. (1994)Cluster Structure and H-Bonding in Native, Substrate-Bound, and 3Fe Forms of Aconitase as Determined by Resonance Raman Spectroscopy. *J. Am. Chem. Soc. 116*, 4053–4061.

(30) Todorovic, S., Leal, S. S., Salgueiro, C. A., Zebger, I., Hildebrandt, P., Murgida, D. H., and Gomes, C. M. (2007)A Spectroscopic Study of the Temperature Induced Modifications on Ferredoxin Folding and Iron-Sulfur Moieties. *Biochemistry 46*, 10733–10738.

(31) Chandramouli, K., Unciuleac, M. C., Naik, S., Dean, D. R., Huynh, B. H., and Johnson, M. K. (2007)Formation and properties of [4Fe-4S] clusters on the IscU scaffold protein. *Biochemistry 46*, 6804–6811.

(32) Fu, W. G., Morgan, T. V., Mortenson, L. E., and Johnson, M. K. (1991)Resonance Raman studies of the [4Fe-4S] to [2Fe-2S] cluster conversion in the iron protein of nitrogenase. *FEBS Lett. 284*, 165–168.

(33) Walters, E. M., Garcia-Serres, R., Naik, S. G., Bourquin, F., Glauser, D. A., Schurmann, P., Huynh, B. H., and Johnson, M. K. (2009) Role of Histidine-86 in the Catalytic Mechanism of Ferredoxin: Thioredoxin Reductase. *Biochemistry 48*, 1016–1024.

(34) Nakamoto, K. (1997) *Infrared and Raman Spectra of Inorganic and Coordination Compounds*, 5th ed., Wiley-Interscience, New York.

(35) Kern, A., Näther, C., and Tuczek, F. (2004)Application of a Universal Force Field to Mixed Fe/Mo-S/Se Cubane and Heterocubane Clusters. 2. Substitution of Iron by Molybenum in $Fe_4(S/Se)_4$ Clusters with Terminal Halide and Thiolate Ligands. *Inorg. Chem. 43*, 5011–5020.

(36) Fukuyama, K., Okada, T., Kakuta, Y., and Takahashi, Y. (2002) Atomic resolution structures of oxidized [4Fe-4S] ferredoxin from *Bacillus thermoproteolyticus* in two crystal forms: Systematic distortion of [4Fe-4S] cluster in the protein. *J. Mol. Biol. 315*, 1155–1166.

(37) Dauter, Z., Wilson, K. S., Sieker, L. C., Meyer, J., and Moulis, J. M. (1997)Atomic resolution (0.94 Å) structure of *Clostridium acidurici* ferredoxin. Detailed geometry of [4Fe-4S] clusters in a protein. *Biochemistry 36*, 16065–16073.

(38) Adman, E., Watenpaugh, K. D., and Jensen, L. H. (1975) NH···S hydrogen bonds in *Peptococcus aerogenes* ferredoxin, *Clostridium pasteurianum* rubredoxin, and *Chromatium* high potential iron protein. *Proc. Natl. Acad. Sci. U.S.A. 72*, 4854–4858.

(39) Giastas, P., Pinotsis, N., Efthymiou, G., Wilmanns, M., Kyritsis, P., Moulis, J. M., and Mavridis, I. M. (2006)The structure of the 2 4Fe-4S ferredoxin from *Pseudomonas aeruginosa* at 1.32-Å resolution: Comparison with other high-resolution structures of ferredoxins and contributing structural features to reduction potential values. *J. Biol. Inorg. Chem. 11*, 445–458.

(40) Yachandra, V. K., Hare, J., Moura, I., and Spiro, T. G. (1983) Resonance Raman Spectra of Rubredoxin, Desulforedoxin, and the Synthetic Analogue $Fe(S_2\text{-}o\text{-}xyl)_2^-$: Conformational Effects. *J. Am. Chem. Soc. 105*, 6455–6461.

(41) Czernuszewicz, R. S., LeGall, J., Moura, I., and Spiro, T. G. (1986)Resonance Raman Spectra of Rubredoxin: New Assignments and Vibrational Coupling Mechanism from Iron-54/Iron-56 Isotope Shifts and Variable Wavelength Excitation. *Inorg. Chem. 25*, 696–700.

(42) Czernuszewicz, R. S., Kilpatrick, L. K., Koch, S. A., and Spiro, T. G. (1994)Resonance Raman Spectroscopy of Iron(III) Tetrathiolate Complexes: Implications for the Conformation and Force Field of Rubredoxin. *J. Am. Chem. Soc. 116*, 1134–1141.

(43) Han, S., Czernuszewicz, R. S., and Spiro, T. G. (1989)Vibrational Spectra and Normal Mode Analysis for [2Fe-2S] Protein Analogues Using ^{34}S, ^{54}Fe, and ^2H Substitution: Coupling of Fe-S Stretch and S-C-C Bending Modes. *J. Am. Chem. Soc. 111*, 3496–3504.

(44) Xiao, Y., Koutmos, M., Case, D. A., Coucouvanis, D., Wang, H., and Cramer, S. P. (2006)Dynamics of an $[Fe_4S_4(SPh)_4]^{2--}$ Cluster Explored via IR, Raman, and Nuclear Resonance Vibrational Spectroscopy (NRVS): Analysis using ^{36}S Substitution, DFT Calculations, and Empirical Force Fields. *Dalton Trans.*, 2192–2201.

(45) Banci, L., Bertini, I., Carloni, P., Luchinat, C., and Orioli, P. L. (1992) Molecular Dynamics Simulations on HiPIP from *Chromatium vinosum* and Comparison with NMR Data. *J. Am. Chem. Soc. 114*, 10683–10689.

(46) Meuwly, M., and Karplus, M. (2004)Theoretical Investigations on *Azotobacter vinelandii* Ferredoxin I: Effects of Electron Transfer on Protein Dynamics. *Biophys. J. 86*, 1987–2007.

(47) Alp, E., Sturhahn, W., Toellner, T. S., Zhao, J., Hu, M., and Brown, D. E. (2002)Vibrational Dynamics Studies by Nuclear Resonant Inelastic X-Ray Scattering. *Hyperfine Interact. 144/145*, 3–20.

(48) Sturhahn, W. (2004)Nuclear resonant spectroscopy. *J. Phys.: Condens. Matter 16*, S497–S530.

(49) Scheidt, W. R., Durbin, S. M., and Sage, J. T. (2005)Nuclear resonance vibrational spectroscopy: NRVS. *J. Inorg. Biochem. 99*, 60–71.

(50) Petrenko, T., Sturhahn, W., and Neese, F. (2007)First-principles calculation of nuclear resonance vibrational spectra. *Hyperfine Interact. 175*, 165–174.

(51) Leu, B. M., Zgierski, M. Z., Wyllie, G. R. A., Scheidt, W. R., Sturhahn, W., Alp, E. E., Durbin, S. M., and Sage, J. T. (2004) Quantitative Vibrational Dynamics of Iron in Nitrosyl Porphyrins. *J. Am. Chem. Soc. 126*, 4211–4227.

(52) Sturhahn, W., Toellner, T. S., Alp, E. E., Zhang, X., Ando, M., Yoda, Y., Kikuta, S., Seto, M., Kimball, C. W., and Dabrowski, B. (1995) Phonon Density of States Measured by Inelastic Nuclear Resonant Scattering. *Phys. Rev. Lett. 74*, 3832–3835.

(53) Sage, J. T., Paxson, C., Wyllie, G. R. A., Sturhahn, W., Durbin, S. M., Champion, P. M., Alp, E. E., and Scheidt, W. R. (2001)Nuclear resonance vibrational spectroscopy of a protein active-site mimic. *J. Phys.: Condens. Matter 13*, 7707–7722.

(54) Appelt, R., and Vahrenkamp, H. (2004)Cyanometal-Substituted Derivatives of the Fe_4S_4 Cluster Core. *Inorg. Synth. 34*, 161–166.

(55) Winter, G. (1973)Iron(II) Halides. *Inorg. Synth. 14*, 101–104.

(56) Menon, A. L., Hendrix, H., Hutchins, A., Verhagen, M., and Adams, M. W. W. (1998)The *δ*-subunit of pyruvate ferredoxin oxidoreductase from *Pyroccus furiosus* is a redox-active, iron-sulfur protein: Evidence for an ancestral relationship with 8Fe-Type ferredoxins. *Biochemistry 37*, 12838–12846.

(57) Fee, J. A., Mayhew, S. G., and Palmer, G. (1971)The Oxidation-Reduction Potentials of Parseley Ferredoxin and Its Selenium-Containing Homolog. *Biochim. Biophys. Acta 245*, 196–200.

(58) Meyer, J. (1986)High-yield chemical assembly of [2Fe-2X] (X = S, Se) clusters into spinach apoferredoxin: Product characterization by resonance Raman spectroscopy. *Biochim. Biophys. Acta 871*, 243–249.

(59) Toellner, T. (2000)Monochromatization of synchrotron radiation for nuclear resonant scattering experiments. *Hyperfine Interact. 125*, 3–28.

(60) Yoda, Y., Yabashi, M., Izumi, K., Zhang, X. W., Kishimoto, S., Kitao, S., Seto, M., Mitsui, T., Harami, T., Imai, Y., and Kikuta, S. (2001) Nuclear resonant scattering beamline at SPring-8. *Nucl. Instrum. Methods Phys. Res., Sect. A 467*, 715–718.

(61) Dowty, E. (1987)Fully automated microcomputer calculation of vibrational spectra. *Phys. Chem. Miner. 14*, 67–79.

(62) Brooks, B. R., Bruccoleri, R. E., Olafson, B. D., States, D. J., Swaminathan, S., and Karplus, M. (1983)CHARMM: A program for macromolecular energy, minimization, and dynamics calculations. *J. Comput. Chem. 4*, 187–217.

(63) Brüschweiler, R. (1995)Collective protein dynamics and nuclear spin relaxation. *J. Chem. Phys. 102*, 3396–3403.

(64) Tama, F., and Sanejouand, Y.-H. (2001)Conformational changes of proteins arising from normal mode calculations. *Protein Eng. 14*, 1–6.

(65) *JAGUAR*, version 7.5 (2008) Schrödinger, LLC, New York.

(66) Frisch, M. J., Trucks, G. W., Schlegel, H. B., Scuseria, G. E., Robb, M. A., Cheeseman, J. R., Zakrzewski, V. G., Montgomery, J. A. J., Stratmann, R. E., Burant, J. C., Dapprich, S., Millam, J. M., Daniels, A. D., Kudin, K. N., Strain, M. C., Farkas, O., Tomasi, J., Barone, V., Cossi, M., Cammi, R., Mennucci, B., Pomelli, C., Adamo, C., Clifford, S., Ochterski, J., Petersson, G. A., Ayala, P. Y., Cui, Q., Morokuma, K., Malick, D. K., Rabuck, A. D., Raghavachari, K., Foresman, J. B., Cioslowski, J., Ortiz, J. V., Stefanov, B. B., Liu, G., Liashenko, A., Piskorz, P., Komaromi, I., Gomperts, R., Martin, R. L., Fox, D. J., Keith, T., Al-Laham, M. A., Peng, C. Y., Nanayakkara, A., Gonzalez, C., Challacombe, M., Gill, P. M. W., Johnson, B., Chen, W., Wong, M. W., Andres, J. L., Head-Gordon, M., Replogle, E. S., and Pople, J. A. (2003) *GAUSSIAN 03*, revision C01, Gaussian Inc., Pittsburgh, PA.

(67) Perdew, J. P., Chevary, J. A., Vosko, S. H., Jackson, K. A., Pederson, M. R., Singh, D. J., and Fiolhais, C. (1991)Atoms, molecules, solids, and surfaces: Applications of the generalized gradient approximation for exchange and correlation. *Phys. Rev. B 46*, 6671–6687.

(68) Olsson, M. H., Ryde, U., and Roos, B. O. (1998)Quantum chemical calculations of the reorganization energy of blue-copper proteins. *Protein Sci. 7*, 2659–2668.

(69) Sigfridsson, E., Olsson, M. H. M., and Ryde, U. (2001)Inner-Sphere Reorganization Energy of Iron-Sulfur Clusters Studied with Theoretical Methods. *Inorg. Chem. 40*, 2509–2519.

(70) Spiro, T., and Czernuszewicz, R. S. (1995)Resonance Raman spectroscopy of metalloproteins. *Methods Enzymol. 246*, 416–460.

(71) Maes, E. M., Knapp, M. J., Czernuszewicz, R. S., and Hendrickson, D. N. (2000)Ligand Conformational Effects on the Resonance Raman Signature of $[Fe_4S_4(SAryl)_4]^{2-}$ Clusters. *J. Phys. Chem. B 104*, 10878–10884.

(72) Xiao, Y., Wang, H., George, S. J., Smith, M. C., Adams, M. W. W., Jenney, F. E., Sturhahn, W., Alp, E. E., Zhao, J., Yoda, Y., Dey, A., Solomon, E. I., and Cramer, S. P. (2005)Normal Mode Analysis of *Pyrococcus furiosus* Rubredoxin via Nuclear Resonant Vibrational Spectroscopy (NRVS) and Resonance Raman Spectroscopy. *J. Am. Chem. Soc. 127*, 14596–14606.

(73) Xiao, Y., Tan, M.-L., Ichiye, T., Wang, H., Guo, Y., Smith, M. C., Meyer, J., Sturhahn, W., Alp, E. E., Zhao, J., Yoda, Y., and Cramer, S. P. (2008)Dynamics of *Rhodobacter capsulatus* [2Fe-2S] Ferredoxin VI and *Aquifex aeolicus* Ferredoxin 5 via Nuclear Resonance Vibrational Spectroscopy (NRVS) and Resonance Raman Spectroscopy. *Biochemistry 47*, 6612–6627.

(74) Georgiadis, M. M., Komiya, H., Chakrabarti, P., Woo, D., Kornuc, J. J., and Rees, D. C. (1992)Crystallographic Structure of the Nitrogenase Iron Protein from *Azotobacter vinelandli. Science 257*, 1653–1659.

(75) Excoffon, P., Laugier, J., and Lamotte, B. (1991)Influence of a Phase Transition in the Solid State on the Structure of a Synthetic Iron-Sulfur Cubane. *Inorg. Chem. 30*, 3075–3081.

(76) Rotsaert, F. A., Pikus, J. D., Fox, B. G., Markley, J. L., and Sanders-Loehr, J. (2003)N-isotope effects on the Raman spectra of Fe_2S_2 ferredoxin and Rieske ferredoxin: Evidence for structural rigidity of metal sites. *J. Biol. Inorg. Chem. 8*, 318–326.

(77) Saito, H., Imai, T., Wakita, K., Urushiyama, A., and Yagi, T. (1991)Resonance Raman Active Vibrations of Rubredoxin. Normal Coordinate Analysis of a 423-Atom Model. *Bull. Chem. Soc. Jpn. 64*, 829–836.

(78) Shoji, M., Koizumi, K., Taniguchi, T., Kitagawa, Y., Yamanaka, S., Okumura, M., and Yamaguchi, K. (2007)Theory of Chemical Bonds in Metalloenzymes III: Full Geometry Optimization and Vibration Analysis of Ferredoxin-Type [2Fe-2S] Cluster. *Int. J. Quantum Chem. 107*, 116–133.

(79) Fiethen, S. A., Staemmler, V., Nair, N. N., Ribas-Arino, J., Schreiner, E., and Marx, D. (2010)Revealing the Magnetostructural Dynamics of 2Fe-2S Ferredoxins from Reduced-Dimensionality Analysis of Antiferromagnetic Exchange Coupling Fluctuations. *J. Phys. Chem. B 114*, 11612–11619.

(80) Marcus, R. A., and Sutin, N. (1985)Electron transfer in chemistry and biology. *Biochim. Biophys. Acta 811*, 265–322.

(81) Jensen, K. P., Ooi, B. L., and Christensen, H. E. (2008)Computational chemistry of modified $[MFe_3S_4]$ and $[M_2Fe_2S_4]$ clusters: Assessment of trends in electronic structure and properties. *J. Phys. Chem. A 112*, 12829–12841.

(82) Reynolds, J. G., Coyle, C. L., and Holm, R. H. (1980)Electron exchange kinetics of $Fe_4S_4(SR)_4^{2-}$-$Fe_4S_4(SR)_4^{3-}$ and $Fe_4Se_4(SR)_4^{2-}$-$Fe_4Se_4(SR)_4^{3-}$ systems: Estimates of the intrinsic self-exchange rate-constant of 4-Fe sites in oxidized and reduced ferredoxins. *J. Am. Chem. Soc. 102*, 4350–4355.

(83) Tan, M. L., Dolan, E. A., and Ichiye, T. (2004)Understanding intramolecular electron transfer in ferredoxin: A molecular dynamics study. *J. Phys. Chem. B 108*, 20435–20441.

(84) Bertero, M. G., Rothery, R. A., Palak, M., Hou, C., Lim, D., Blasco, F., Weiner, J. H., and Strynadka, N. C. J. (2003)Insights into the respiratory electron transfer pathway from the structure of nitrate reductase A. *Nat. Struct. Biol. 10*, 681–687.

(85) Sazanov, L. A., and Hinchliffe, P. (2006)Structure of the Hydrophilic Domain of Respiratory Complex I from *Thermus thermophilus. Science 311*, 1430–1436.

(86) Pochapsky, T. C., Kostic, M., Jain, N., and Pejchal, R. (2001)Redox-Dependent Conformational Selection in a $Cys_4Fe_2S_2$ Ferredoxin. *Biochemistry 40*, 5602–5614.

(87) Morales, R., Charon, M. H., Kachalova, G., Serre, L., Medina, M., Gomez-Moreno, C., and Frey, M. (2000)A redox-dependent interaction between two electron-transfer partners involved in photosynthesis. *EMBO Rep. 1*, 271–276.

(88) Calzolai, L., Zhou, Z. H., Adams, M. W. W., and LaMar, G. N. (1996)Role of Cluster-Ligated Aspartate in Gating Electron Transfer in the Four-Iron Ferredoxin from the Hyperthermophilic Archaeon *Pyrococcus furiosus. J. Am. Chem. Soc. 118*, 2513–2514.

(89) Yabashi, M., Tamasaku, K., Kikuta, S., and Ishikawa, T. (2001)X-ray monochromator with an energy resolution of 8×10^{-9} at 14.41 keV. *Rev. Sci. Instrum. 72*, 4080–4083.

(90) Röhlsberger, R. (2004) Methods and instrumentation. In *Nuclear Condensed Matter Physics with Synchrotron Radiation: Basic Principles, Methodology and Applications*, pp 37–65, Springer, Berlin.

(91) Shenoy, G. K., and Rohlsberger, R. (2008)Scientific opportunities in nuclear resonance spectroscopy from source-driven revolution. *Hyperfine Interact. 182*, 157–172.

(92) Kim, K.-J., Shvyd'ko, Y., and Reiche, S. (2008)A Proposal for an X-Ray Free-Electron Laser Oscillator with an Energy-Recovery Linac. *Phys. Rev. Lett. 100*, 244802.